Materials and Design 199 (2021) 109441

Contents lists available at ScienceDirect

Materials and Design

journal homepage: www.elsevier.com/locate/matdes

# Experimental study of the influence of operational and geometric variables on the powders produced by close-coupled gas atomisation

Ernesto Urionabarrenetxea [a,b,*], Alejo Avello [a,b], Alejandro Rivas [b], José Manuel Martín [a,b]

[a] CEIT-Basque Research and Technology Alliance (BRTA), Manuel Lardizabal 15, 20018 Donostia / San Sebastián, Spain
[b] Universidad de Navarra, Tecnun, Manuel Lardizabal 13, 20018 Donostia / San Sebastián, Spain

## HIGHLIGHTS

- Close-coupled gas atomisation is a highly reproducible manufacturing method.
- The gas-to-metal volumetric flow rates ratio is more relevant than the commonly employed mass flow rates ratio.
- Determining the minimum superheat is complex and helium requires higher superheats.
- Atomising with higher melt superheats can favour the formation of aggregates.
- Kishidaka's modified correlation reliably predicts the median particle size of the powders.

## GRAPHICAL ABSTRACT

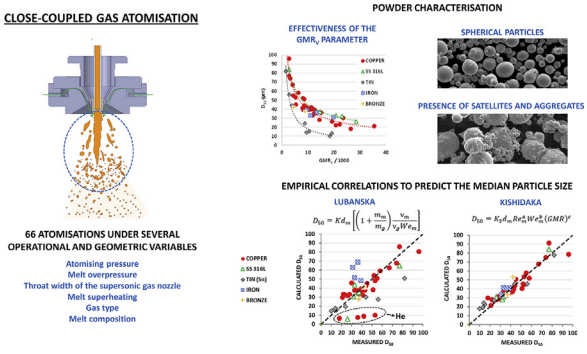


## ARTICLE INFO

*Article history:*
Received 10 November 2020
Received in revised form 9 December 2020
Accepted 24 December 2020
Available online 28 December 2020

*Keywords:*
Close-coupled gas atomisation
Superheat
Helium
Particle size distribution
Empirical correlation
Kishidaka

## ABSTRACT

The effect of several operational and geometric variables on the particle size distribution of powders produced by close-coupled gas atomisation is analysed from a total of 66 experiments. Powders of three pure metals (copper, tin and iron) and two alloys (bronze Cu-15 wt% Sn and stainless steel SS 316 L) have been produced. Nitrogen, argon and helium were used as atomising gases. It is shown that the gas-to-metal ratio of volume flow rates ($GMR_V$) is more relevant than the ratio of mass flow rates (GMR) in order to analyse the effect of atomisation variables on the particle size. Kishidaka's equation, originally proposed for water atomisation, is modified to predict the median particle size in gas atomisation. The accuracy of the new equation is compared with that of Lubanska, and Rao and Mehrotra. Kishidaka's modified empirical correlation is the most accurate in predicting the median particle size of the powders produced in this work. The morphology of the produced powders is studied by scanning electron microscopy (SEM) and it is observed that the melt superheat can play an important role in the aggregation of fine particles (< 10 μm), which increases the fraction of large particles (> 100 μm).



*Abbreviations:* $d_m$, Melt stream diameter; $D_{10}$, $D_{50}$ and $D_{90}$, 10th, 50th and 90th percentile of the particle size distribution; $E_{max}$, Maximum absolute error; $E_{mean}$, Mean absolute error; GMR, Gas-to-metal mass flow rates ratio; $GMR_V$, Gas-to-metal volumetric flow rates ratio; $K_1$, Lubanska's correlation's adjustable parameter; $K_2$ and m, Rao and Mehrotra's correlation's two adjustable parameters; $K_3$, a, b and c, Kishidaka's correlation's four adjustable parameters; $L_o$, Throat width of the gas nozzle; $m_g$, Gas mass flow rate; $m_m$, Melt mass flow rate; P, Atomising pressure; $Re_m$, Dimensionless Reynolds number; $R^2$ and $R^2_{adj}$, R-squared and adjusted R-squared of nonlinear regression models; $T_m$, Melting or liquidus temperature; $U_g$, Velocity of the gas in the atomisation zone; $We_m$, Dimensionless Weber's number; ΔP, Melt overpressure; ΔT, Melt superheat; $\mu_m$, Dynamic viscosity of the melt; $\nu_g$, Kinematic viscosity of the gas; $\nu_m$, Kinematic viscosity of the melt; $\rho_g$, Density of the gas; $\rho_m$, Density of the melt; $\sigma_{LN}$, Geometric standard deviation of the log-normal distribution; $\sigma_m$, Surface tension of the melt.

* Corresponding author at: CEIT-Basque Research and Technology Alliance (BRTA), Manuel Lardizabal 15, 20018 Donostia / San Sebastián, Spain.
*E-mail addresses:* eugomez@ceit.es (E. Urionabarrenetxea), alavello@ceit.es (A. Avello), arivas@tecnun.es (A. Rivas), jmmartin@ceit.es (J.M. Martín).

https://doi.org/10.1016/j.matdes.2020.109441

## 1. Introduction

The use of a gas to break up a molten stream is termed gas atomisation and is an effective method of producing fine spherical metal powders. The principle of this process is to transfer kinetic energy from a high-speed gas jet to a liquid metal stream, which in turn becomes unstable. The gas expanding around the melt causes a dramatic depressurisation and the disintegration of the liquid into droplets, which finally solidify as metal particles. The gas atomiser designs most commonly employed in industry are the close-coupled and free-fall types. The gas exit is next to the melt nozzle exit in close-coupled atomisation, while a distance varying from 10 to 30 cm is maintained between them in the free-fall atomisation units. Despite the drawbacks of backflow and freeze-up, which do not normally occur during free-fall atomisation, close-coupled atomisers are able to produce finer powders because the proximity of the gas and melt streams favours energy transfer [9].

Scientific research on gas atomisation can be divided into experimental and numerical studies. Since the computational power and mathematical models that existed decades ago were scarce, the most practical tool was to conduct experiments. Ayers and Anderson [5] confirmed that the use of higher gas pressures favoured the obtaining of finer powders. Ünal [33] showed that helium produced the finest powders, argon gave the coarsest and nitrogen yielded powder sizes in-between. Furthermore, he fitted the particle size distribution to a log-normal distribution and deduced that the mean particle size was directly proportional to the square root of the melt mass flow. Snyder et al. [28] worked with different liquids and reported that the particle size increased when liquids with a higher viscosity and surface tension were sprayed. Later, the use of visualisation systems such as Schlieren's photography, high-speed cinematography and holography revealed additional phenomena occurring during the process. Ünal [33] stressed that atomisers producing longer supersonic gas plumes allowed for the obtaining of powders with finer size distributions, since they favoured a more effective secondary atomisation. Mates et al. [16] observed that increasing the pressure of the atomising gas produced longer supersonic plumes. Mates and Settles [17] demonstrated that the convergent atomisers always provided strongly under-expanded flows, while over-expanded or very slightly under-expanded flows were obtained with convergent-divergent gas nozzles. Due to the improved expansion achieved with the convergent-divergent nozzles, they claimed that these atomisers were more efficient. Their photographs demonstrated that the secondary atomisation persists well away from the region where primary atomisation occurs, therefore global atomisation is not limited to a region close to the impingement point between both flows [18]. A rapid variation of the instantaneous melt flow has been observed by different researchers employing different visualisation techniques such as high-speed cinematography [31] or the Particle Image Velocimetry (PIV) technique [22]. This chaotic nature of the interaction between both phases in a real atomisation affects the particle size distribution of the resulting powder. Ting et al. [32] postulated that this fluctuation of the melt flow could be related to changes of the aspiration pressure in the melt feed tube due to the presence of the liquid. Their pulsatile atomisation model predicts fluctuating aspiration pressures between suction and overpressure values which create variations in the liquid flow rate. This would also explain why the melt flow rates in close-coupled atomisers tend to be lower than in free-fall atomisers, even when high suctions are measured. Miller et al. [21] had previously shown that there was little correlation between the measurements of the aspiration pressure and the resulting liquid flow rates. Nowadays, the simplest correlation between the atomising variables and the particle size distribution states that a higher gas-to-melt mass flow rates ratio (GMR) contributes to produce a finer powder as demonstrated for Ni-based alloys by Ting et al. [32], for tin by Ünal [34], for aluminium by Saleh et al. [25] or for copper by Anderson et al. [3]. When the gas pressure rises, in addition to increasing the gas mass flow rate, the melt flow will usually decrease. Both effects help produce finer powders, since the GMR parameter increases. Superheating the melt decreases its viscosity and prolongs the solidification time, which subsequently produces finer powders, too [23]. Since the calculation capacity of modern computers provides more precision and reduces the required computational time, the interest for applying Computational Fluid Dynamics (CFD) techniques to the analysis of the gas atomisation process is increasing considerably. Simulations reveal details of the flow that are not experimentally accessible, but which have an impact on the powder properties. In recent years, certain researchers have made important advances in the modelling of the primary and secondary atomisation stages, along with the solidification of liquid droplets during their flight time in the atomisation chamber. The works of Zeoli and Gu [39], Wei et al. [38] and Hanthanan Arachchilage et al. [10] are examples of these types of numerical studies. However, simulating this kind of multiphase flow is still challenging due to the complex interaction between two fluids with very different physical properties. As a result, most articles are mainly focused on modelling the gas flow dynamics in the absence of the liquid metal to gain a better understanding of key aspects of the process.

Using the accumulated experimental evidence, several authors have tried to link the median particle size of a powder ($D_{50}$) with the atomisation conditions through empirical correlations. Lubanska's Eq. [14] is probably the most well-known and most commonly quoted for free-fall, ring-like atomisers due to its reasonable accuracy under various experimental conditions. In order to make Lubanska's correlation applicable to more general conditions (e.g. close-coupled atomisers with sonic-supersonic-sonic transitions), Rao and Mehrotra [24] proposed substituting Lubanska's exponent 0.5 by an adjustable parameter "m":

$$D_{50} = K_2 d_m \left[ \left( 1 + \frac{m_m}{m_g} \right) \frac{\nu_m}{\nu_g We_m} \right]^m \tag{1}$$

$$We_m = \frac{d_m \rho_m U_g^2}{\sigma_m} \tag{2}$$

where $d_m$ is the melt stream diameter; $m_m$ and $m_g$ are the mass flow rates of melt and gas, respectively; $\nu_m$ and $\nu_g$ are the kinematic viscosities of melt and gas, respectively; $We_m$ is the dimensionless Weber's number; $U_g$ is the gas velocity in the atomisation zone; $\rho_m$ the density of the melt; and $\sigma_m$ its surface tension. $K_2$ and "m" are two parameters calculated by fitting the experimental data from a given atomiser with eq. (1).

Kishidaka [12] proposed a dimensionless equation for water atomisation, including four adjustable parameters ($K_2$, "a", "b", and "c"), where the ratio $D_{50}/d_m$ is a function of the Reynold's number ($Re_m$), the Weber's number ($We_m$), and the ratio of water-to-melt mass flow rates. The same equation may be applied to gas atomisation by substituting the velocity and mass flow rate of water for the same properties of the gas:

$$D_{50} = K_3 d_m \, Re_m^{\,a} We_m^b (GMR)^c \tag{3}$$

$$Re_m = \frac{d_m \rho_m U_g}{\mu_m} \tag{4}$$

where $\mu_m$ is the dynamic viscosity of the melt.

The characteristics of the powders produced by close-coupled gas atomisation depend on different operational variables, geometrical parameters and physicochemical properties of gas and melt. In this work, a systematic set of experiments is conducted to analyse the effect of the gas inlet pressure, the superheat of the melt, the throat width of the supersonic nozzle, the overpressure applied to the melt, the gas type and the melt composition on the particle size distribution. Moreover, the proclaimed great influence of GMR parameter is

re-examined in detail. Finally, the accuracy of the above mentioned empirical equations to predict $D_{50}$ is compared.

## 2. Experimental procedure

Experimental atomisations were performed in a two-in-one small-scale research atomisation unit (PSI model HERMIGA 75/3VI). The atomiser is a close-coupled type with a convergent-divergent annular-slit gas nozzle. The raw material was melted in a ceramic crucible using an induction furnace. The atomisation unit allows for the pressurisation of the melting chamber up to 1.5 bar in order to enhance the melt flow from the crucible to the atomisation chamber. The batch size is nearly 3 kg. Melting was conducted under high purity argon. The atomisation chamber was also evacuated and purged with argon to minimise oxidation. The diameter of the melt delivery tube used in the experiments was 2.5 mm. In this study, the following variables were investigated:

- Gas atomisation pressure (P, varied between 10 and 60 bar).
- Overpressure applied to the melt (ΔP, from 0.25 to 0.4 bar).
- Gas supersonic nozzle's throat width ($0.6{\cdot}L_o$, $0.77{\cdot}L_o$ and $0.91{\cdot}L_o$). The throat width $L_o$ the characteristic length used in the CFD simulations presented elsewhere [35]).
- Melt superheat (ΔT, varied between 25 and 500 °C).
- Atomising gas (nitrogen, helium and argon).
- Melt composition: Three pure metals (copper, tin and iron) and two alloys (bronze Cu-15 wt% Sn and stainless steel SS 316 L) were used as raw materials.

The overpressure applied to the melt takes into account both the aspiration pressure measured in the melt feed tube and the pressurisation of the melting chamber. For example, if an overpressure applied to the melt of 0.25 bar is desired and a suction of 0.10 bar is measured in the melt feed tube, the melting chamber is pressurised to 0.15 bar. However, if an overpressure of 0.10 bar is measured in the melt feed tube, the melt chamber is pressurised to 0.35 bar.

The physicochemical properties of both the atomising gases and the melts at different temperatures are listed in Tables 1 and 2, respectively. The raw materials were chosen to cover a wide range of physicochemical properties relevant to atomisation (density, viscosity, surface tension and solidification temperature range). In this way, it is possible to evaluate their effect on the characteristics of the atomised powders. Furthermore, they are not highly volatile materials (compared, for example, with Zn or Mn) and are not highly reactive (compared, for example, with Al, Mg or Ti).

The $m_g$ value is known from CFD simulations under steady state conditions [35], whereas $m_m$ is calculated dividing the weight of the powder by the atomisation time. Consequently, the mass flow rates, the volume flow rates and the corresponding ratios used in this article are always average values, i.e. they are not instantaneous values. After each atomisation, the particle size distribution was measured by sieve analysis following the MPIF standard #5 ([20]). For fine powders (with 90th percentile < 80 μm), the laser diffraction equipment Sympatec HELOS (model H0852; dry dispersion unit RODOS; vibratory feeding unit VIBRI; compressed air inlet pressure of 1 bar) was employed. The statistical descriptors used to compare the distributions are the 10th percentile ($D_{10}$), the median particle size ($D_{50}$) and the 90th percentile ($D_{90}$). Additionally, since the experimental data fit well to the log-normal distribution, the geometric standard deviation of the log-normal distribution ($\sigma_{LN}$) is reported. The morphology of the particles was assessed qualitatively via the Philips XL30CP Scanning Electron Microscopy (SEM). The as-atomised powders have been divided into size fractions by sieving in order to analyse shape changes with particle size.

**Table 1**
Physicochemical properties of the different gases at normal conditions (1 atm, 20 °C) [4].

| Property | Nitrogen | Helium | Argon |
|---|---|---|---|
| Density (kg/m$^3$) | 1.165 | 0.166 | 1.661 |
| Specific heat (J/(kg·K)) | 979 | 5193 | 520 |
| Thermal conductivity (W/(m·K)) | 0.0242 | 0.152 | 0.0158 |
| Dynamic viscosity (Pa·s) | 1.663e-5 | 1.99e-5 | 2.125e-5 |
| Molecular weight (kg/mol) | 28.01 | 4.00 | 39.95 |

**Table 2**
Physicochemical properties of the melts at different temperatures.

| Material | Melting or liquidus temperature | Superheat | Density | Dynamic viscosity | Surface tension |
|---|---|---|---|---|---|
| | $T_m$ (°C) | ΔT (°C) | $\rho_m$ (kg/m$^3$) | $\mu_m$ (Pa·s) | $\sigma_m$ (N/m) |
| Cu | 1083 | | a) | b) | a) |
| | | 0 | 8000 | 0.00468 | 1.303 |
| | | 25 | 7980 | 0.00461 | 1.297 |
| | | 55 | 7956 | 0.00450 | 1.290 |
| | | 100 | 7920 | 0.00436 | 1.280 |
| | | 117 | 7904 | 0.00429 | 1.275 |
| | | 200 | 7840 | 0.00410 | 1.257 |
| | | 350 | 7720 | 0.00398 | 1.225 |
| | | 500 | 7600 | 0.00310 | 1.188 |
| Sn | 232 | | a) | b) | a) |
| | | 0 | 6980 | 0.00196 | 0.560 |
| | | 74 | 6935 | 0.00174 | 0.553 |
| | | 186 | 6867 | 0.00155 | 0.543 |
| | | 200 | 6858 | 0.00152 | 0.542 |
| | | 500 | 6675 | 0.00145 | 0.515 |
| Fe | 1535 | | a) | c) | a) |
| | | 0 | 7030 | 0.00591 | 1.872 |
| | | 165 | 6885 | 0.00460 | 1.799 |
| Bronze (Cu-15% Sn) | 960 | | d) | b) | e) |
| | | 0 | 7847 | 0.00466 | 0.850 |
| | | 149 | 7709 | 0.00406 | 0.834 |
| | | 444 | 7504 | 0.00340 | 0.833 |
| SS 316 L | 1440 | | f) | g) | g) |
| | | 0 | 7105 | 0.00500 | 1.784 |
| | | 260 | 6728 | 0.00405 | 1.530 |

a) Extracted from Iida and Guthrie [11].
b) Extracted from Tan et al. [30].
c) Extracted from Sato et al. [26].
d) Calculated from the data for pure copper and pure tin [11].
e) Extracted from Lee et al. [13].
f) Extracted from Fukuyama et al. [8].
g) Extracted from Zhang and Zhang [40].

## 3. Results and discussion

A total of 66 experiments under different atomising conditions have been performed, as shown in the Appendix. Using the characterisation results of these powders, subsequent sections discuss the reproducibility of the process, the influence of the different variables and, finally, the accuracy of three empirical correlations to predict the median particle size.

### 3.1. Study of the reproducibility of the process

Before drawing any conclusions about the influence of each operational or geometric variable, it is essential to verify that those powders produced under the same nominal atomisation conditions have equivalent particle size distributions. Multiple experiments with copper under the same conditions were performed to study the reproducibility of the process (see atomisations Cu-1 to Cu-11 in the Appendix). Table 3 shows the mean and standard deviation of the gas flow rate ($m_g$), the melt flow rate ($m_m$), the resulting GMR and the main descriptors of the eleven particle size distributions. When the atomisations are

performed under the same conditions, the gas flow rate is constant. However, the control of the melt flow rate in close-coupled atomisation is quite difficult because of the aspiration effect on the melt feed tube, contrary to what occurs in free-fall atomisation. In order to control the melt flow rate, the aspiration pressure in the melt feed tube was measured before each atomisation and the pressurisation of the melting chamber was regulated accordingly until identical overpressures were applied to the melt. This methodology allowed for better process control, thus providing low standard deviations of melt flow rate and GMR, and consequently of $D_{50}$ and $\sigma_{LN}$. The range of $D_{50}$ is only 7 μm (from 35 to 42 μm) and $\sigma_{LN}$ takes values between 1.9 and 2.1, which are typical for gas atomised powders [1]. Therefore, it can be stated that the atomisations present a high reproducibility.

### 3.2. Effect of the atomisation variables on the particle size distribution of the powders

#### 3.2.1. The atomising pressure

The inlet pressure of the gas is one of the parameters with the strongest influence on the particle size distribution. In order to analyse the effect of this operational variable, ten experiments with copper have been performed using nitrogen at 6 different inlet pressures (runs from Cu-12 to Cu-21 in the Appendix). Fig. 1 illustrates the three different situations observed. At the lowest pressure (10 bar), droplets are so coarse that they reach the collector without solidifying, thereby producing a deposition instead of loose powder. At the highest pressure (60 bar), the melt freezes at the tip, so the atomisation is blocked. Loose powder was obtained between these two limits.

In agreement with the literature, Fig. 2 indicates that finer powders are achieved by increasing the atomising pressure, since the $D_{50}$ value decreases [29]. As $\sigma_{LN}$ values decrease, powders with narrower particle size distributions are obtained too. CFD techniques have revealed that an increase of the inlet pressure provides a higher gas mass flow rate, higher velocities in the atomisation chamber and a longer supersonic plume [36], which explains the observed trend. However, the tendency is not conclusive due to the great disparity of liquid flow rates obtained at 50 bar. As indicated in the Appendix, the overpressure applied to the melt was not controlled in these initial experiments.

Fig. 3 shows that a better correlation is obtained when the same data is displayed as a function of GMR, proving that this is a more fundamental variable than the inlet pressure. Higher GMR values contribute to obtaining finer powders with narrower particle size distributions ($D_{50}$ and $\sigma_{LN}$ decrease with this ratio). A further factor was not revealed by the simulations, since they were carried out in the absence of the liquid phase; when the atomising pressure is increased, the melt flow rate is reduced and, consequently, smaller GMR ratios than expected are obtained.

#### 3.2.2. The melt overpressure

The overpressure applied to the melt affects the resulting melt flow rate. The influence of this operational variable has been studied by performing the atomisations Cu-22 to Cu-29 listed in the Appendix. Two atomisations have been carried out at each inlet pressure, the difference between them being the applied overpressure (either 0.25 or 0.4 bar). Fig. 4 shows that the melt flow rate increases with the overpressure. This effect is more evident at lower inlet pressures of the gas. Moreover, it is observed again that the melt flow rate tends to decrease when the atomising pressure is increased, even if the same overpressure is used. Since the overpressure is regulated considering both the aspiration pressure in the melt feed tube and the pressurisation of the melt chamber, it should be constant irrespective of the atomising pressure. This variation has been also reported by other authors such as Miller et al. [21], which confirms that a precise control of the melt flow rate is challenging in close-coupled gas atomisation. The reduction of the melt flow rate with the atomising pressure can be due to different factors. On the one hand, CFD simulations showed that the gas flow generates a recirculation zone or wake under the melt nozzle and that there is a stagnation point near the melt exit hole. With higher inlet pressures, the size of the wake is reduced and the pressure at the stagnation point is increased (Urionabarrenetxea et al., 2013). The combination of both factors may hinder the flow of the melt from the crucible, thus decreasing its mass flow rate. On the other hand, the aspiration pressure can only be measured in the absence of the melt stream; the presence of the liquid metal during the atomisation will also affect this variable.

Figs. 5 and 6 display the median particle size and $\sigma_{LN}$ of the atomised powders as a function of the inlet pressure and the GMR, respectively, for both overpressures. In Fig. 5, it is observed that higher overpressures produce slightly coarser powders and the experimental data of $D_{50}$ lay in two different lines. On the other hand, Fig. 6 demonstrates that the experimental data of $D_{50}$ from both overpressures lay on a single line when they are represented as a function of GMR. This fact suggests that GMR is a more fundamental variable than the inlet pressure or the melt overpressure. These latter operational variables affect the particle size indirectly through their effect on the mass flow rates of the melt and the gas. The correlation of $\sigma_{LN}$ with GMR is also slightly better than with the atomising pressure. In general, the lower the GMR values, the lower the particle size and the width of the distribution.

#### 3.2.3. The throat width of the convergent-divergent gas nozzle

The throat width of the supersonic nozzle is considered to be one of the most critical geometric parameters of the gas atomiser. Atomisations Cu-12 to Cu-21 have been performed using the $0.6{\cdot}L_o$ gas nozzle whereas the $0.77{\cdot}L_o$ gas nozzle has been used in the atomisations Cu-22 to Cu-29. The median particle size of these powders as a function of the inlet pressure is compared in Fig. 7, where finer powders are commonly obtained at the same atomising pressure when the throat width of $0.77{\cdot}L_o$ is employed. Differences of up to 20 μm can be noticed in the $D_{50}$ of the powders produced at the same inlet pressure. Similar to what occurs with the atomising pressure, an increase of this geometric variable provides higher mass flow rates of gas, higher velocities in the atomisation chamber and longer supersonic plumes, so the fragmentation process is enhanced [35]. It is observed in Fig. 8 that the experimental data of $D_{50}$ and $\sigma_{LN}$ correlate better once again with GMR than with the inlet pressure. However, if the data of $D_{50}$ at the lowest GMR values are carefully examined (inset in Fig. 8), it is detected that some powders produced under practically identical GMR present quite different median particle sizes. Consequently, there must be other variables, apart from GMR, that affect the particle size distribution of gas atomised powders.

When the simultaneous influence of the inlet pressure and the throat width on the gas flow dynamics was studied numerically, it was observed that the predicted mass flow rates and velocities always varied proportionally, regardless of the specific combination of values of these two variables. The smaller the amount of gas introduced into the atomisation chamber, the smaller its velocity and vice versa [35]. Therefore, it was suggested that the simplest option to compare powders produced with different gas atomisers was to use the mass flow rate (or the velocity) as the main variable of the gas. Fig. 9 shows $D_{50}$ as a function of GMR for different values of the mass flow rate (or the velocity) of the gas. The values of the velocities in the legend correspond to the maximum velocities in the axis of the computational domain

**Table 3**
Gas and melt mass flow rates, GMR ratio and main parameters of the particle size distributions of the Cu-1 to Cu-11 powders (Cu, gas $N_2$, $P = 55$ bar, $\Delta P = 0.25$ bar, throat width = $0.6{\cdot}L_o$ and $\Delta T = 117$ °C).

| | $m_g$ (g/s) | $m_m$ (g/s) | GMR | $D_{10}$ (μm) | $D_{50}$ (μm) | $D_{90}$ (μm) | $\sigma_{LN}$ |
|---|---|---|---|---|---|---|---|
| Mean | 41.74 | 25.31 | 1.69 | 14 | 39 | 100 | 1.96 |
| Standard deviation | 0 | 3.97 | 0.27 | 3 | 2 | 11 | 0.06 |

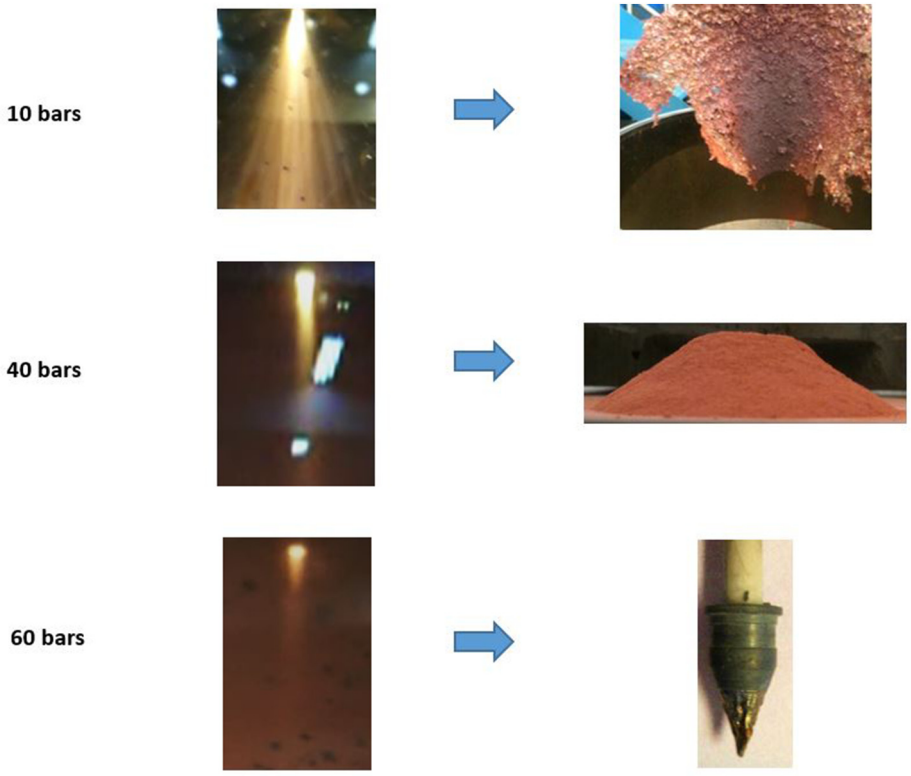


**Fig. 1.** Photographs taken during the experiments and the resulting products (Cu, gas $N_2$, throat width = 0.77·$L_o$ and ΔT = 200 °C).

calculated numerically. It is observed that the use of low gas flow rates always provides low GMR values, so it is very difficult to obtain fine powders under these conditions. Thanks to this graph, it is also clear that finer powders are obtained at the same GMR ratio when the mass flow rate (or the velocity) of the atomising gas is increased. The arrows in Fig. 9 visually indicate this effect. This point can be explained by considering that higher gas flow rates also mean higher velocities and longer supersonic plumes, so they enable more kinetic energy to be transferred to the melt. The influence of this variable gradually decreases at higher values. CFD simulations have already demonstrated that there is a point at which a systematic increase of the gas flow rate barely affects the velocity of the gas. Consequently, even if the melt flow rate could be adjusted to achieve identical GMR values with two very different gas flow rates, the produced powder would present different particle size distributions due to the influence of the gas velocity, which is not considered inside the GMR. Therefore, it is fair to conclude that the GMR parameter does not fully capture the complexity of the atomisation process.

*3.2.4. The melt superheat*

The superheat of the melt decreases its density, viscosity and surface tension and prolongs the solidification time of the droplets, thus enhancing the secondary atomisation stage. In order to analyse the influence of the superheat on the particle size distribution, five atomisations with identical processing variables and increasing superheat temperatures are compared in this section (atomisations Cu-30 to Cu-33 and Cu-16 listed in the Appendix). No powder was produced in the experiment with a superheat of 25 °C because the melt froze at the exit of the melt nozzle. The minimum superheat for a successful atomisation was 55 °C. The reduction in melt viscosity associated with higher superheats hardly affected the resulting metal mass flow rate. Therefore, the GMR values obtained in these experiments were

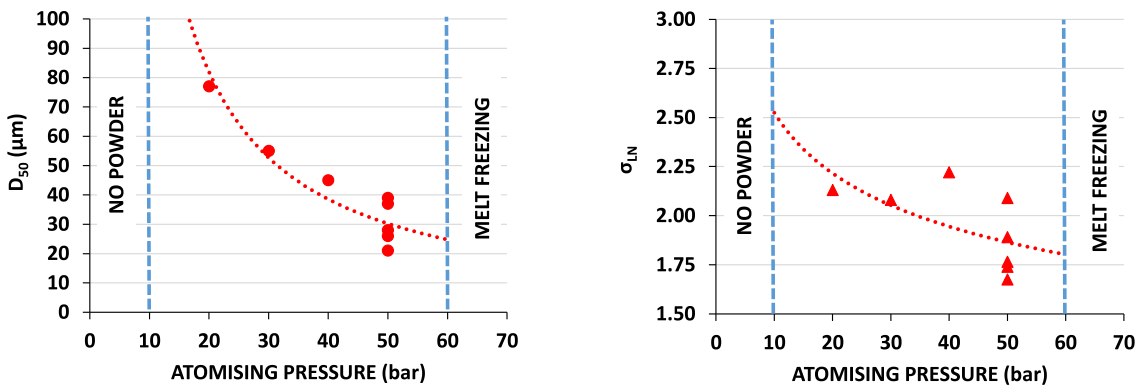


**Fig. 2.** $D_{50}$ (left) and $\sigma_{LN}$ (right) of Cu powders as a function of the inlet $N_2$ pressure (throat width = 0.77·$L_o$ and ΔT = 200 °C).

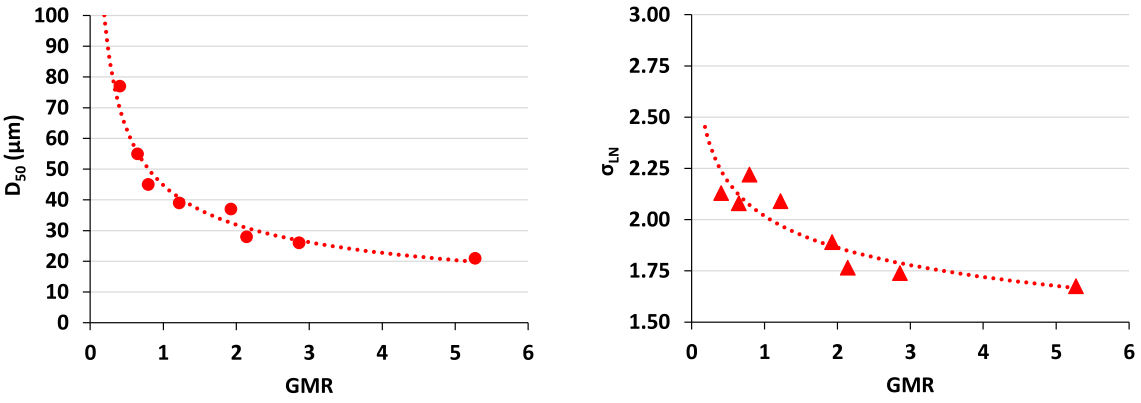


**Fig. 3.** $D_{50}$ (left) and $\sigma_{LN}$ (right) of Cu powders as a function of GMR (gas $N_2$, $P$ = 10–60 bar, throat width = 0.77·$L_o$ and ΔT = 200 °C).

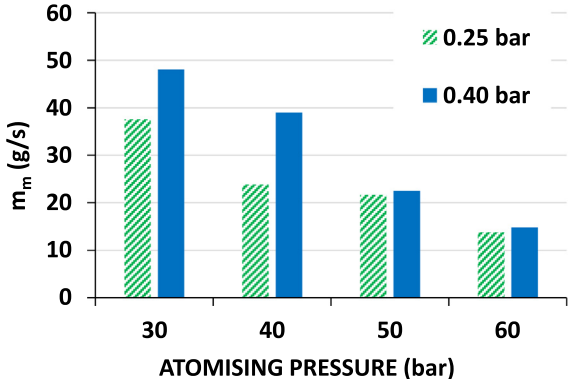


**Fig. 4.** Measured melt mass flow rates ($m_m$) in Cu atomisations as a function of the inlet $N_2$ pressure at two different overpressures ΔP = 0.25 bar or 0.4 bar (throat width = 0.6·$L_o$ and ΔT = 200 °C).

practically identical and the differences found in the particle size distribution are directly linked to the superheat. As shown in Fig. 10, the copper powders show a decrease of $D_{50}$ and $D_{90}$ with the superheat for values below 100 °C. However, no further refinement beyond this value is noted. Ünal [33] also observed that a higher superheat slightly reduced the particle size of the powders. Somewhat wider particle size distributions are also measured when the superheat is increased, as $\sigma_{LN}$ increases in Fig. 10.

Powders produced by gas atomisation present a near-spherical particle morphology. Some satellites are usually observed attached to the surface of coarse particles [15] and some powders could also present aggregates of fine particles [27]. These defects are produced by the re-entry of fine particles into the atomisation zone during the process [37]. Satellites are formed when small solid particles weld on a large semisolid particle, whereas aggregates are formed when many small semisolid particles weld together. The height and diameter of the atomisation chamber could affect their formation [29]. The presence of satellites and aggregates is undesirable because they widen the particle size distribution, increase the median particle size, increase the irregularity of the powders, and reduce the effective packing and flowability of the resulting powders. Moreover, they can become an important source of defects in final components.

Fig. 11 displays micrographs of several size fractions separated by sieving two copper powders produced using different superheats. By inspecting the copper powders produced with a superheat of 200 °C, it is observed that the particles of the finest fractions have a predominantly spherical shape and a smooth surface, and they are practically free of surface defects. However, the particles of the coarsest fractions are more irregular, their surface is not smooth, they show a high number of satellites on their surface and few fine particles aggregates are visible. In contrast, the copper powder obtained with a superheat of 500 °C presents a much higher concentration of aggregates, even in the fine fractions. In other words, the tendency to form satellites and aggregates increases with the superheat. The previously remarked lack of further refinement when higher superheats are employed (see Fig. 10) can be related to this increasing aggregation of fine particles. Although the number of large spherical particles is reduced, the formation of aggregates is favoured with higher melt pouring temperatures. For this reason, lower $D_{90}$ values are not actually obtained when the superheat is increased. The aggregation also explains the slight increase of $\sigma_{LN}$ in Fig. 10.

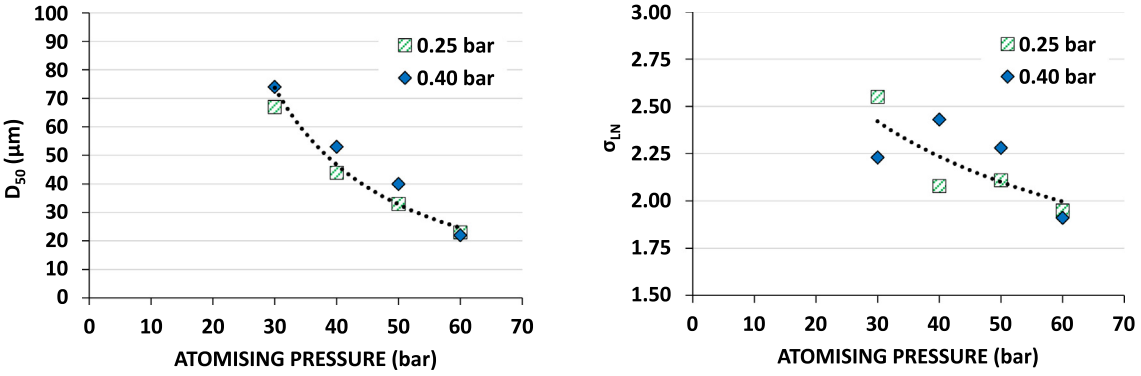


**Fig. 5.** $D_{50}$ (left)and $\sigma_{LN}$ (right) of Cu powders as a function of the inlet $N_2$ pressure at two different overpressures ΔP = 0.25 bar or 0.4 bar (throat width = 0.6·$L_o$ and ΔT = 200 °C).

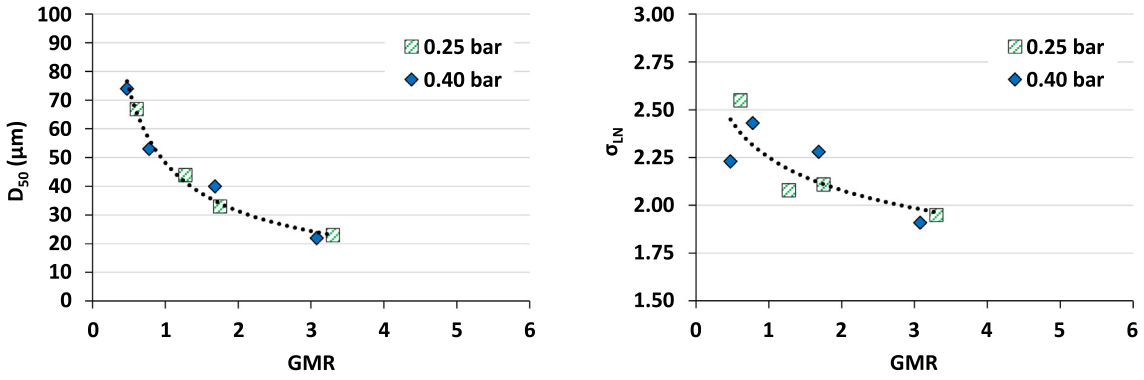


**Fig. 6.** $D_{50}$ (left) and $\sigma_{LN}$ (right) of Cu powders as a function of GMR at two different overpressures $\Delta P = 0.25$ bar or 0.4 bar (gas $N_2$, $P = 30$–60 bar, throat width $= 0.6 \cdot L_o$ and $\Delta T = 200$ °C).

Another interesting feature related to the melt superheat is detected by comparing the particle size distributions of the tin powders produced in atomisations Sn-6 and Sn-8. In these experiments, two different superheats were employed (74 and 500 °C, respectively), but practically identical GMR values of 3.2 were obtained, so any difference in the particle size distributions is linked to the melt pouring temperature. Fig. 12.a reveals that an increase of the melt superheat slightly reduces the median particle size. However, the decrease of $D_{90}$ is more important. This means that the number of tin coarse particles is clearly reduced and, as a result, a narrower particle size distribution is also obtained. The same trend is observed when comparing the powders of atomisations Sn-3 (186 °C), Sn-5 (74 °C) and Sn-7 (200 °C), in which fairly similar GMR values between 1.47 and 1.76 were obtained (see Fig. 12.b).

The same refinement observed with tin powders was not observed with copper due to the detected aggregation. In fact, the micrographs in Fig. 13 show that tin powders do not show aggregates and they also present fewer satellites.

Fig. 14 shows the morphology of an iron powder. It is corroborated that this material does not form aggregates of particles as copper does. The micrographs also illustrate that coarse particles present a higher amount of satellites attached to their surface than fine particles. This is explained by considering that the gas atomised particles of different size cool at different rates, typically in the range from $10^4$ to $10^6$ K/s [6]. The coarse particles need more time to solidify, so the probability of colliding with the fine particles dragged by the internal recirculation loops is clearly enhanced.

*3.2.5. The atomising gas*

Previous atomisations were conducted with nitrogen. Ten additional experiments, atomisations Cu-34 to Cu-43, have been performed with argon and helium at increasing inlet pressures. Although many different inert gases can be used as atomising fluids, the most common ones are nitrogen, argon and helium. Due to its lower cost, nitrogen is the preferred choice. When atomising materials reactive with nitrogen, argon is usually employed. The use of helium is expensive, but its high thermal conductivity enhances the cooling rate of the particles, helping to obtain amorphous structures [2]. As shown in the Appendix, the runs with helium at 50 and 60 bar using a superheat of 200 °C were unsuccessful because the melt solidified at the nozzle exit. Two photographs of a copper freeze around the melt nozzle are presented in Fig. 15, showing that the strong cooling power of helium caused the solidification of the liquid melt during the process. Additionally, the $\sigma_{LN}$ of the powders produced with helium at 30, 40 and 45 bar using a superheat of 200 °C is much higher than those obtained in the rest of experiments, suggesting a premature solidification of the droplets. When the superheat was increased to 350 °C (experiment Cu-43), the melt did not freeze even though the atomisation was conducted with helium at 60 bar. Moreover, the resulting powder showed a normal $\sigma_{LN}$ value of 1.99. Therefore, it is corroborated that higher superheats are necessary when atomising with helium.

Fig. 16 shows the variation of $D_{50}$ and $\sigma_{LN}$ of all copper powders with respect to the GMR parameter. The abnormally high values of $\sigma_{LN}$ obtained using helium with a superheat of 200 °C stand out (encircled). Finer powders and narrower particle size distributions are obtained when GMR increases for the three atomising gases. It is worth remarking the great influence of the atomising gas on the particle size distribution here. For a given value of GMR, helium provides the finest powder and the narrowest distribution, argon yields the coarsest powder and the widest distribution, and nitrogen gives values in-between. This trend is directly related to the molecular weight of the gases, since helium is the lightest, argon is the heaviest and nitrogen is in-between. This suggests that the GMR parameter, despite its usefulness

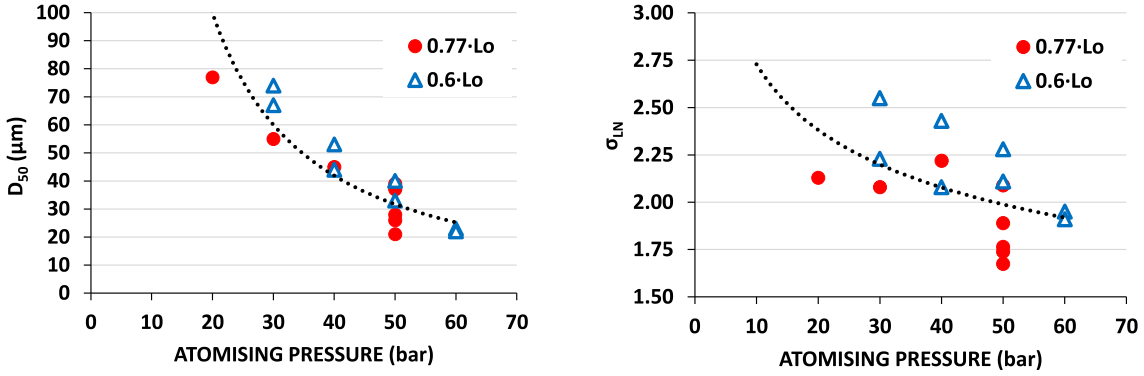


**Fig. 7.** $D_{50}$ (left) and $\sigma_{LN}$ (right) of the Cu powders as a function of the inlet $N_2$ pressure for two different throat widths $= 0.6 \cdot L_o$ or $0.77 \cdot L_o$ ($\Delta T = 200$ °C).

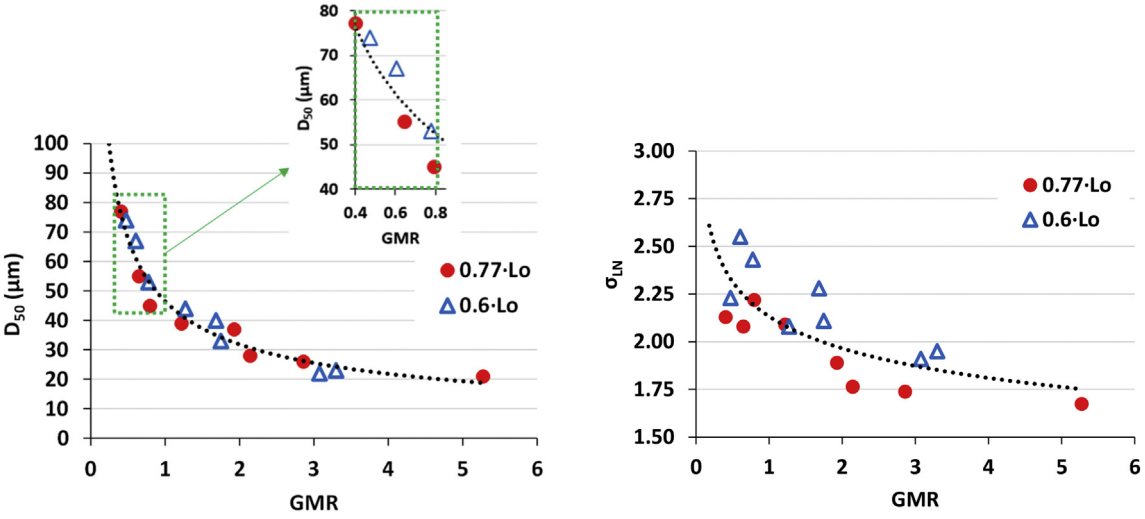


**Fig. 8.** $D_{50}$ (left) and $\sigma_{LN}$ (right) of Cu powders as a function of GMR for two different throat widths = 0.6·$L_o$ or 0.77·$L_o$ (gas $N_2$, $P$ = 20–60 bar and $\Delta T$ = 200 °C).

when comparing powders produced under different atomising conditions, does not capture such essential differences in the atomisations carried out with different gases.

CFD simulations predicted that the mass flow rate of argon is slightly superior to that of nitrogen, whereas the helium mass flow rate is the lowest under the same atomising conditions. However, the opposite trend was obtained for the volumetric flow rates. Whereas the volumetric flow rates of argon and nitrogen were relatively similar, the simulation with helium predicted a consumption of gas that was practically three times larger (Urionabarrenetxea et al., 2013). These facts suggest that the particle size may correlate better with the gas-to-metal volume flow rates ratio ($GMR_V$) than with the gas-to-metal mass flow rates ratio (GMR). The $GMR_V$ parameter is easily calculated through the following expression:

$$GMR_V = GMR \cdot \frac{\rho_m}{\rho_g} \tag{5}$$

The density values of the atomising gas ($\rho_g$) under normal conditions and the melt ($\rho_m$) at the furnace temperature are listed in Tables 1 and 2, respectively. When $D_{50}$ and $\sigma_{LN}$ are represented as a function of $GMR_V$, the graphs of Fig. 17 are obtained. These descriptors of the particle size distribution correlate very well with $GMR_V$, even if the powders were produced under different conditions, including the use of different atomising gases. The only data that does not properly match is that coming from the atomisations with helium using a superheat of 200 °C due to the premature freezing of the melt, as previously explained.

Dunkley [7] proposed almost two decades ago that the analysis of atomisation on the basis of a dimensionless volume gas/volume metal would prove more interesting in the future. This work clearly confirms Dunkley's hypothesis and the usefulness of the $GMR_V$ parameter.

The use of the average $GMR_V$ as a fundamental variable to describe the gas atomisation process exhibits several limitations. Firstly, while GMR is constant throughout the process, $GMR_V$ closely depends on

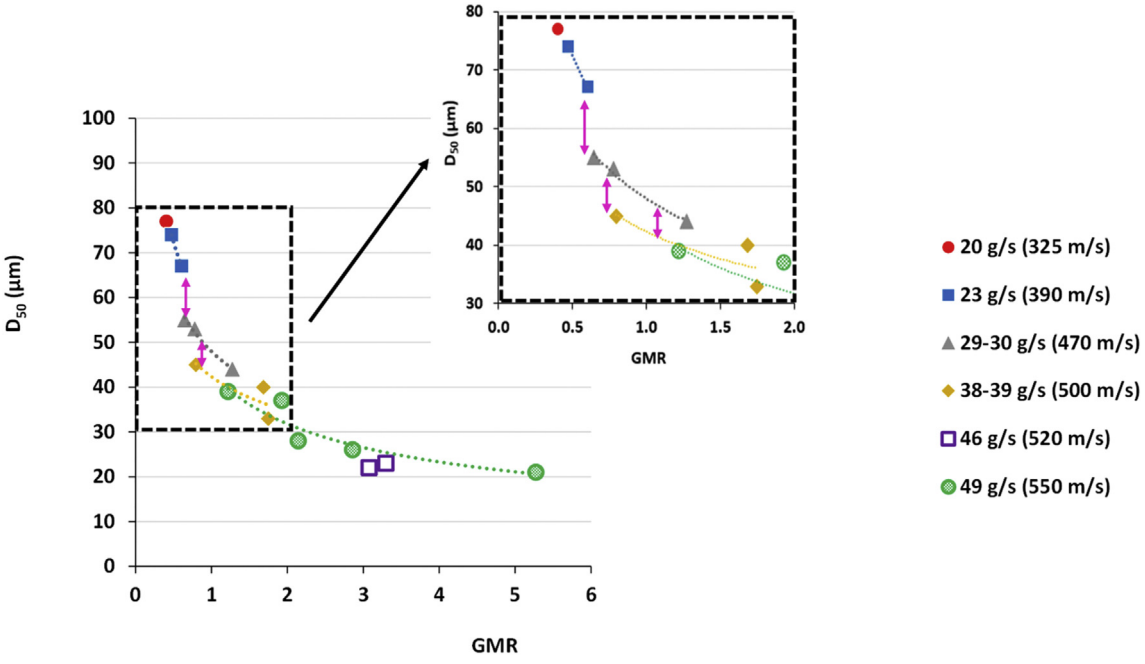


**Fig. 9.** $D_{50}$ of the Cu powders as a function of GMR obtained with different gas mass flow rates (or velocities) (gas $N_2$, $P$ = 20–60 bar, throat width = 0.6·$L_o$ or 0.77·$L_o$ and $\Delta T$ = 200 °C).

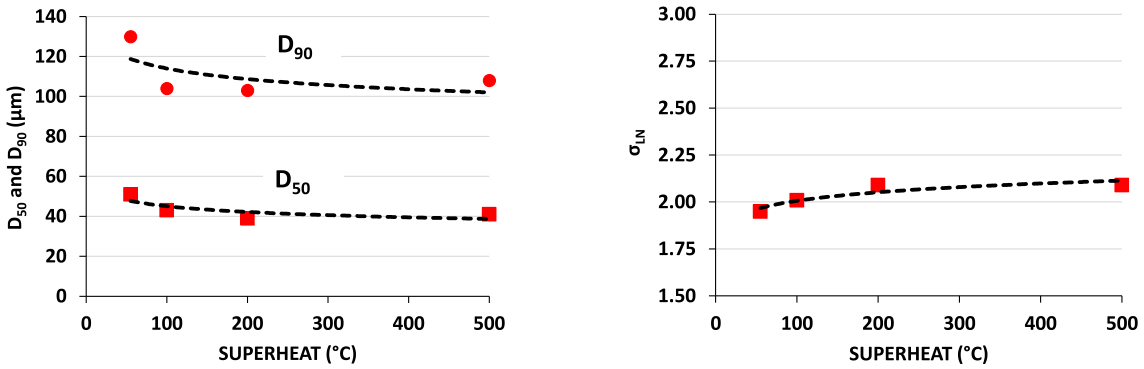


**Fig. 10.** $D_{50}$ and $D_{90}$ (left) and $\sigma_{LN}$ (right) of Cu powders as a function of melt superheat (gas $N_2$, $P = 50$ bar, $\Delta P = 0.25$ bar and throat width $= 0.77\ L_o$).

the density of the gas, which in turn depends on the average (or "effective") temperature of the gas in the atomisation zone. This effective temperature is very difficult to obtain either experimentally or by numerical methods. So far, there is not reliable data or model [41]. In this study, the problem was overcome by calculating the density at the same temperature of 20 °C in all the experiments. Nevertheless, it is obvious that the real effective temperature should be much higher. Additionally, it is not the same for the different gases, since the effective heat transfer coefficient depends on the velocity field and other properties such as viscosity, heat capacity and thermal conductivity, which are gas dependent.

Secondly, the influence of the gas velocity, which was remarked in section 3.2.3, must be discussed in more detail. One of the reasons why $GMR_V$ seems to be a better variable than GMR is because it somehow includes the influence of the gas velocity. The average volumetric flow rate in $GMR_V$ is equal to the cross-sectional area of the gas flow multiplied by the average velocity magnitude. CFD simulations predicted that helium would give much higher velocities and longer supersonic plumes than nitrogen and argon, so it may enable the transfer of more kinetic energy to the melt and produce finer powders (Urionabarrenetxea et al., 2013). The reason for this is related to the high sonic velocity of helium, which practically triples the sonic velocities of nitrogen and argon (for example, at a temperature of 0 °C, the sonic velocity of helium, nitrogen and argon is 970, 334 and 319 m/s, respectively). Excluding the atomisations with helium using a superheat of 200 °C, Fig. 17 shows that the hypothetical curve for helium (red diamonds) may be located slightly below the nitrogen line due to its higher velocity. On the other hand, the curve for argon (green triangles) may be located slightly above due to its lower velocity. Of course, these small jumps may be also attributed to the fact that the calculated average $GMR_V$ does not account for the different effective temperature of the gases. Nevertheless, the possible influence of the different velocity fields circumscribed to the atomisation zone should not be excluded in future analyses.

Despite the limitations explained in the previous paragraphs, the use of $GMR_V$ as a main variable to describe the principle trend of particle

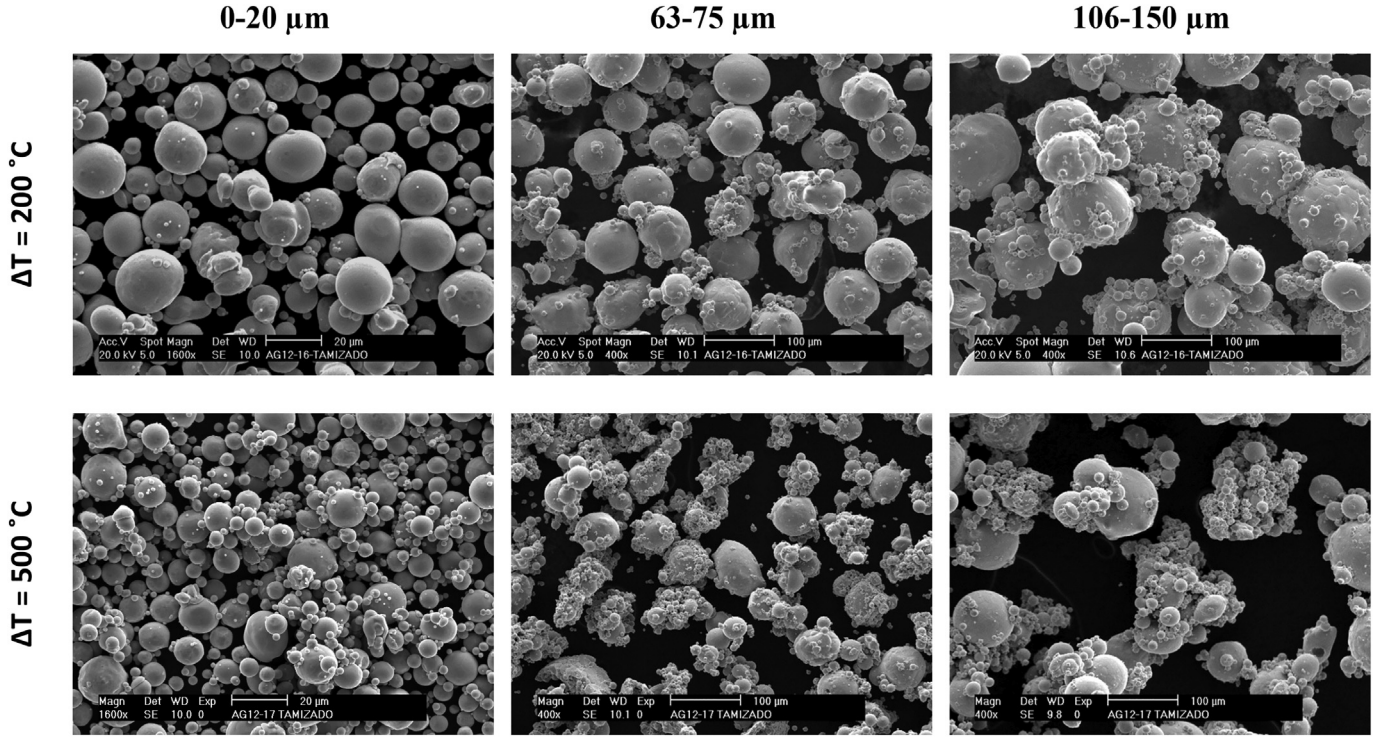


**Fig. 11.** Micrographs from different size fractions of two Cu powders obtained applying different melt superheats (gas $N_2$, $P = 50$ bar, $\Delta P = 0.25$ bar and throat width $= 0.77\ L_o$).

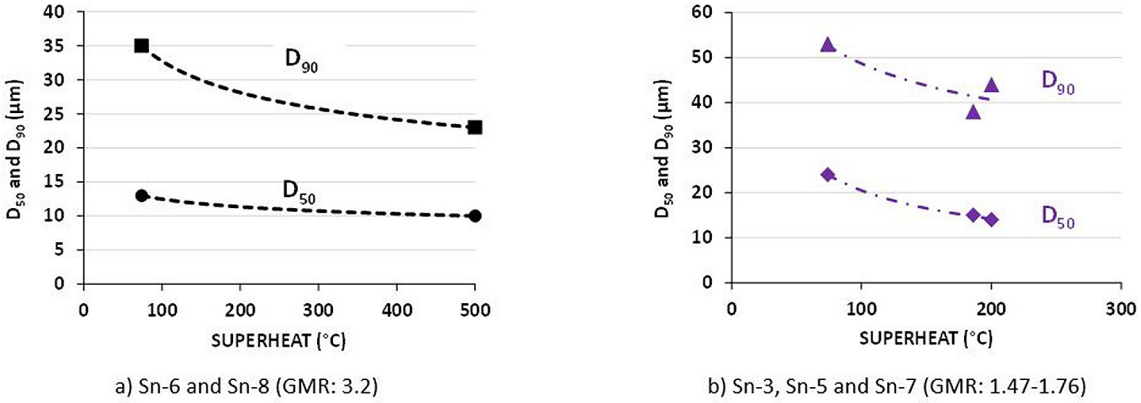


**Fig. 12.** $D_{50}$ and $D_{90}$ of Sn powders as a function of melt superheat.

size in gas atomisation is endorsed by the clear correlation shown in Fig. 17.

*3.2.6. Effect of melt composition*

The results presented in previous sections have allowed for analysis of the influence of the most important operational and geometric variables of the gas atomisation process during the production of copper powders. However, it is a well-known fact that the physicochemical properties of the melt also affect the resulting particle size distribution. Therefore, the influence of melt composition has been studied by performing other experiments using tin, iron, bronze Cu-15 wt% Sn and stainless steel SS 316 L, as shown in the Appendix. The three iron atomisations using helium (experiments Fe-5, Fe-6 and Fe-7) were blocked due to melt freeze-up even at a low inlet pressure of 30 bar (see Fig. 18). The applied superheat of 165 °C is clearly insufficient, but it was not possible to increase it due the melting equipment's limitations.

Fig. 19 shows $D_{50}$ and $\sigma_{LN}$ as a function of the new parameter $GMR_V$. The influence of $GMR_V$ is more noticeable at lower values, i.e. the slope of the curves decreases gradually with this ratio until it barely affects the particle size. For the same $GMR_V$, tin produces the finest powders with the narrowest distributions, whereas the SS 316 L gives the coarsest with the widest distributions, and copper values are in-between. This trend correlates with the surface tension and the viscosity of the melts reported in Table 2, i.e. the fragmentation of the melt is easier (or requires less energy transfer from the gas) when the surface tension and viscosity are lower.

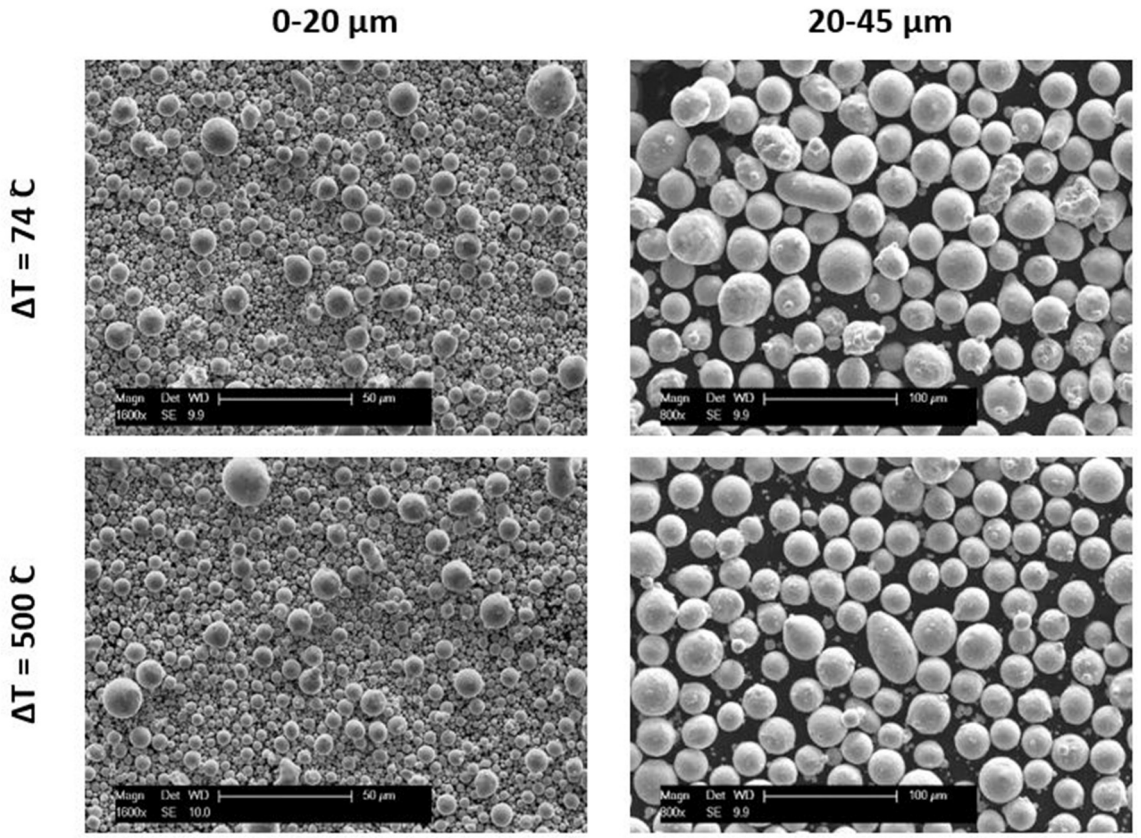


**Fig. 13.** Micrographs from different size fractions of two Sn powders obtained applying different melt superheats (gas $N_2$, $P = 60$ bar, $\Delta P = 0.25$ bar and throat width $= 0.6 \cdot L_o$).

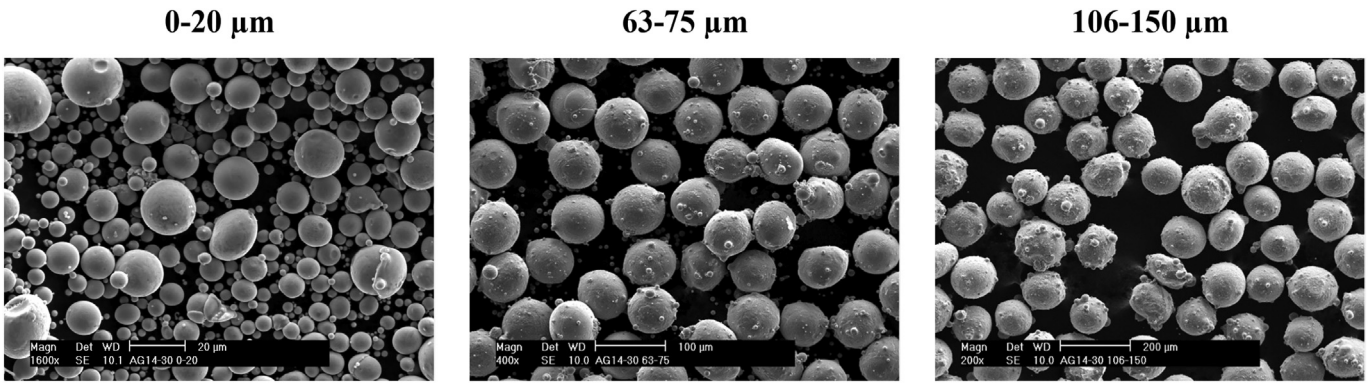


**Fig. 14.** Micrographs of an iron powder (gas $N_2$, P = 60 bar, ΔP = 0.25 bar, throat width = 0.6·$L_o$ and ΔT = 165 °C).

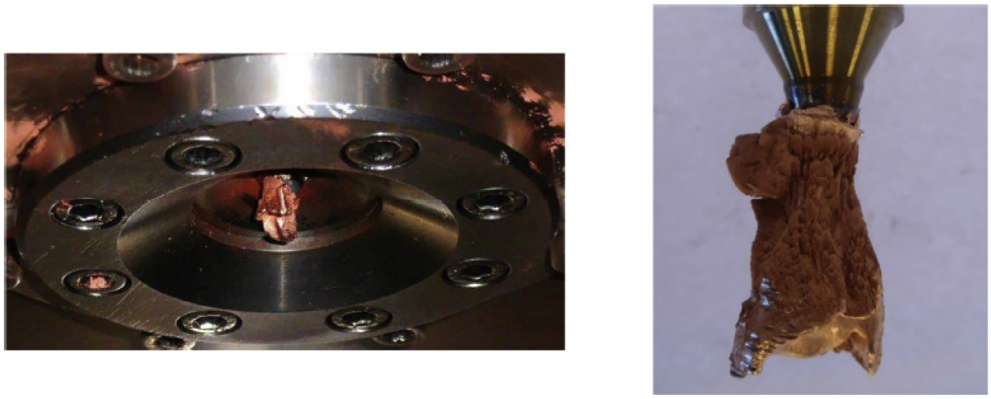

**Fig. 15.** Atomisation blocked due to Cu freeze around the melt nozzle (gas He, *P* = 50–60 bar, ΔP = 0.25 bar, throat width = 0.6·$L_o$ and ΔT = 200 °C).

### 3.3. Empirical correlations

In this section, the accuracy of Lubanska's, Rao and Mehrotra's and Kishidaka's modified empirical correlations to predict the median particle size of the powders, depending on the atomising conditions, is analysed. The following data is required in order to use these expressions:

- The melt stream diameter $d_m$, which coincides with the diameter of the melt nozzle and is 2.5 mm in all the experiments.
- The melt and gas mass flow rates ($m_m$ and $m_g$, respectively) of each atomisation, which are listed in the previous Appendix.
- The kinematic viscosities of both fluids ($\nu_m$ and $\nu_g$), which have been calculated from the values in Tables 1 and 2, since $\nu_m = \frac{\mu_m}{\rho_m}$ and $\nu_g = \frac{\mu_g}{\rho_g}$.
- The melt density ($\rho_m$), dynamic viscosity ($\mu_m$) and surface tension ($\sigma_m$), which are given in Table 2.
- The gas velocity, which has been obtained from CFD simulations. Table 4 shows the velocities used in the calculations as a function

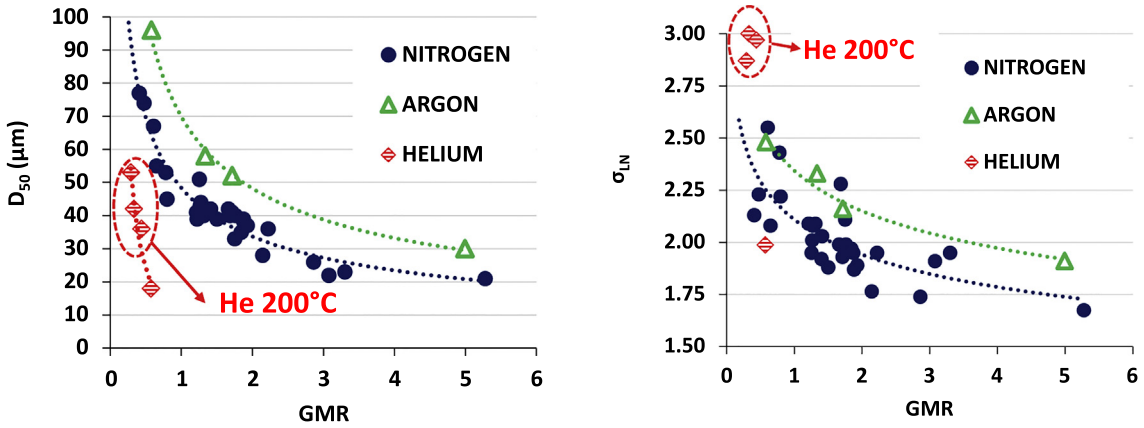


**Fig. 16.** $D_{50}$ (left) and $\sigma_{LN}$ (right) of Cu powders atomised with different gases as a function of GMR (*P* = 10–60 bar, ΔP = 0.25 bar or 0.4 bar, throat width = 0.6·$L_o$ or 0.77 $L_o$ and ΔT = 55–200 °C).

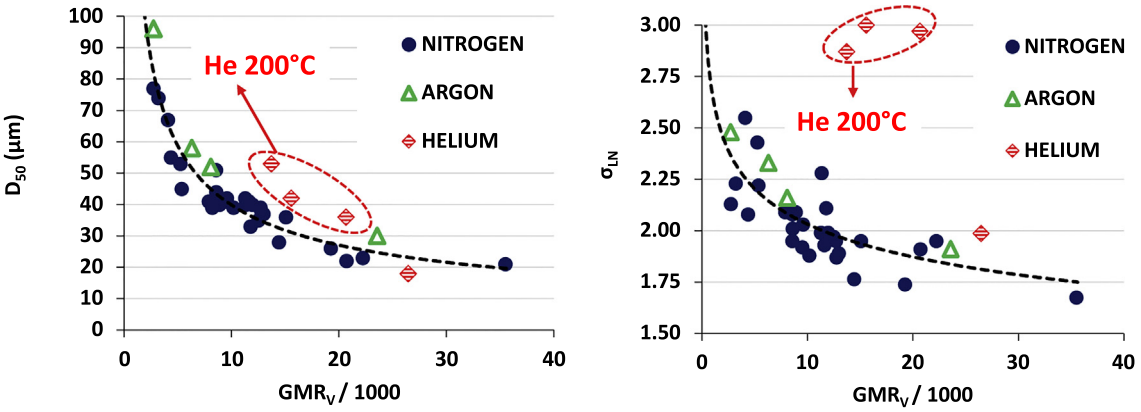


**Fig. 17.** $D_{50}$ (left) and $\sigma_{LN}$ (right) of Cu powders atomised with different gases as a function of $GMR_V$ (P = 10–60 bar, ΔP = 0.25 bar or 0.4 bar, throat width = 0.6·$L_o$ or 0.77 $L_o$ and ΔT = 55–200 °C).


**Fig. 18.** Atomisations blocked due to Fe freeze around the melt nozzle, conducted at different inlet He pressures (ΔP = 0.25 bar, throat width = 0.6·$L_o$ and ΔT = 165 °C).

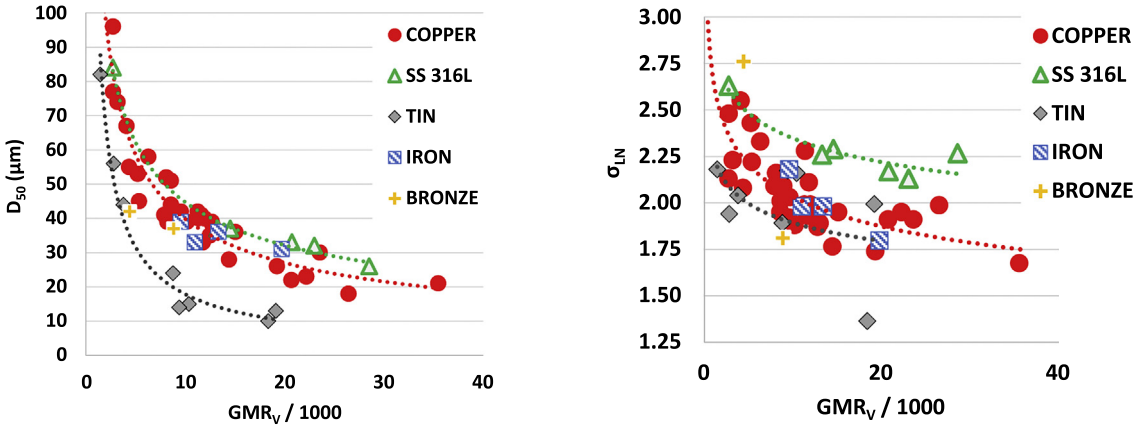


**Fig. 19.** $D_{50}$ (left) and $\sigma_{LN}$ (right) as a function of $GMR_V$ of Cu, Sn, Fe, bronze Cu-15 wt% Sn and SS 316 L powders produced under diverse atomising conditions (see Appendix).

**Table 4**
Gas velocities used in the empirical correlations.

| Nitrogen | | Argon | | Helium | |
|---|---|---|---|---|---|
| $m_g$ (g/s) | $U_g$ (m/s) | $m_g$ (g/s) | $U_g$ (m/s) | $m_g$ (g/s) | $U_g$ (m/s) |
| 19.6 | 325 | 29.8 | 325 | 8.9 | 1090 |
| 22.8 | 390 | 39.8 | 355 | 11.8 | 1180 |
| 29.4–30.4 | 470 | 49.7 | 375 | 16.6 | 1250 |
| 34.1 | 485 | 59.6 | 380 | 17.8 | 1290 |
| 37.9–39.2 | 500 | 68.2 | 400 | | |
| 41.7 | 510 | | | | |
| 45.5 | 520 | | | | |
| 49.0 | 550 | | | | |
| 52.0 | 570 | | | | |

of the gas mass flow rate. These velocities are the maximum values calculated in the axis of the computational domain.

Lubanska's correlation contains one adjustable parameter ($K_1$), Rao and Mehrotra's two parameters ($K_2$ and "m") and Kishidaka's correlation modified to be used in gas atomisation has four parameters ($K_3$, "a", "b" and "c"). These parameters are calculated by fitting the experimental data using the least squares regression techniques available in Matlab software [19]. Table 5 presents the values of the different parameters which provide the best fitting, mean and maximum absolute errors, and the coefficients $R^2$ and $R^2_{adj}$, which measure the goodness of the adjustment. The main difference between $R^2$ and $R^2_{adj}$is that the $R^2_{adj}$ takes into account the number of parameters used to achieve the adjustment, while $R^2$ does not. For this reason, it is more convenient to compare the accuracy of the three correlations using $R^2_{adj}$. The median particle size of the different powders is compared with the values calculated using the empirical correlations in Fig. 20.

Lubanska's correlation fails to predict the median particle size of the powders atomised with helium. Moreover, the fitting obtained for tin and iron powders is not good, either. As a result, the value of $R^2_{adj}$ is very low. Despite the fact that the mean error made with this equation is only around 9 μm, high errors of up to 43 μm are observed. The value of $K_1$ obtained in this study is far from those reported by Lubanska [14], which were between 40 and 50, because this parameter is characteristic of each atomisation unit. The errors and $R^2_{adj}$ value obtained with the correlation of Rao and Mehrotra are quite similar to those of Lubanska. The mean error is the same, the maximum error is slightly reduced and the $R^2_{adj}$ value is slightly higher, but still low. Rao and Mehrotra [24] reported values between 6 and 12 for the parameter $K_2$ and between 0.26 and 0.3 for the parameter m, similar to the values obtained in this case. Finally, Kishidaka's modified correlation provides the best predictions. The mean and maximum errors are reduced up to 4 and 18 μm, respectively. The sign of each of the parameters is also consistent with the physical meaning of the corresponding dimensionless numbers. Finally, $R^2_{adj}$ is close to 0.9, showing a significant association between the variables of the model and the median particle size. Consequently, it is evident that Kishidaka's modified equation is the most reliable to predict the median particle size of the powders produced with the atomisation unit used in this study.

**Table 5**
Values of the parameters that best fit the experimental data and the obtained absolute errors.

| Correlation | Parameters | $E_{mean}$ (μm) | $E_{max}$ (μm) | $R^2$ | $R^2_{adj}$ |
|---|---|---|---|---|---|
| Lubanska | $K_1 = 123.82$ | 9 | 43 | 0.365 | 0.353 |
| Rao and Mehrotra | $K_2 = 7.33$ m = 0.34 | 9 | 36 | 0.428 | 0.408 |
| Kishidaka | $K_3 = 42.09$ a = −0.34 b = −0.18 c = −0.42 | 4 | 18 | 0.885 | 0.877 |

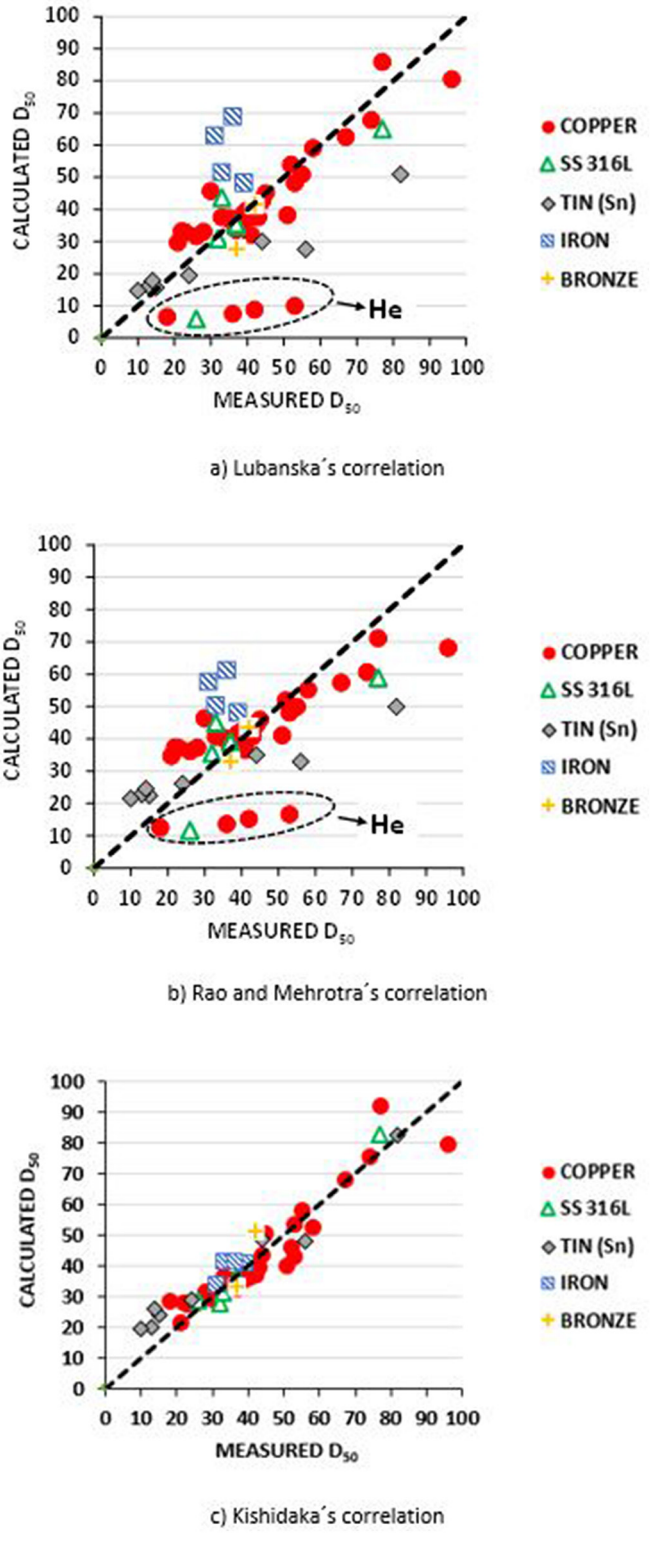


**Fig. 20.** Calculated v.s. experimental $D_{50}$ values (see Appendix for the experimental conditions).

Due to the good correlation observed which describes the trend of particle size in gas atomisation with the $GMR_V$, new correlations may be proposed using this parameter in the future. It could lead to simpler correlations with less parameters. However, it would be convenient to first address the limitations discussed in section 3.2.5.

## 4. Conclusions

a) It is demonstrated the reproducibility of gas atomisation using close-coupled, convergent-divergent gas nozzles, i.e. the ability of the process to produce metal powders with similar properties.
b) It is shown that the $GMR_V$ parameter is a more significant variable than the GMR parameter to describe the variation of the particle size distribution when other indirect variables are modified (e.g. the inlet pressure, the throat area of the gas nozzle, the melt overpressure or the atomising gas).
c) Determining the minimum superheat to produce powder by gas atomisation is a complex problem that depends on many different factors such as the atomising gas, the inlet pressure, the mass flow rates of melt and gas, the materials, the design of the atomiser or even the melt liquidus temperature. However, the experiments conducted in this study allow for the stablishing of some general rules. For example, a minimum superheat of 100 °C is sufficient in the case of copper atomised with nitrogen, but a superheat of 200 °C is low with helium because the efficiency of the process is clearly reduced or the atomisation is stopped due to freeze-up.
d) Atomising with higher melt superheats reduces the number of large spherical particles in the powders, so the $D_{90}$ value should decrease. However, this effect is not detected with copper powders because the use of a higher superheat with this material also favours the formation of fine particles aggregates.
e) For the same $GMR_V$, finer powders with narrower particle size distributions are produced when the viscosity and surface tension of the melt is lower.
f) Kishidaka's empirical correlation, modified to be applied in gas atomisation, is the most reliable equation to predict the median particle size of the powders produced in this work.
g) The particles from the finest fractions have a predominantly spherical shape, a smooth surface and are practically free of surface defects. However, the particles of the coarser fractions are more irregular, their surface is not smooth, they show a high number of satellites and include a significant fraction of aggregates of fine particles.

## Credit author statement

**Ernesto Urionabarrenetxea**: Methodology, Investigation, Formal analysis, Visualization, Writing - Original Draft. **Alejo Avello**: Formal analysis, Writing - Review & Editing. **Alejandro Rivas**: Methodology, Formal analysis, Conceptualization, Writing - Review & Editing, Supervision. **José Manuel Martín**: Methodology, Conceptualization, Writing - Review & Editing, Supervision, Funding acquisition.

## Declaration of Competing Interest

The authors declare that they have no known competing financial interests or personal relationships that could have appeared to influence the work reported in this paper.

## Acknowledgements

This work was supported by the Spanish Government ("Programa Estatal de I+D+i Orientada a los Retos de la Sociedad del Ministerio de Economía, Industria y Competitividad", contract N° MAT2017-88957-R).

## Appendix

Details of the atomisation runs performed as well as the mass flow rates of both the gas and the melt, the resulting GMR and the main parameters of the particle size distributions of the produced powders.

| Atomisation | Gas | P (bar) | Throat width | ΔP* (bar) | ΔT (°C) | $m_g$ (g/s) | $m_m$ (g/s) | GMR | $D_{10}$ (μm) | $D_{50}$ (μm) | $D_{90}$ (μm) | $\sigma_{LN}$ |
|---|---|---|---|---|---|---|---|---|---|---|---|---|
| Cu-1 | $N_2$ | 55 | $0.6{\cdot}L_o$ | 0.25 | 117 | 41.7 | 31.8 | 1.31 | 13 | 40 | 109 | 2.09 |
| Cu-2 | $N_2$ | 55 | $0.6{\cdot}L_o$ | 0.25 | 117 | 41.7 | 22.7 | 1.84 | 9 | 35 | 83 | 1.97 |
| Cu-3 | $N_2$ | 55 | $0.6{\cdot}L_o$ | 0.25 | 117 | 41.7 | 22.2 | 1.88 | 13 | 38 | 90 | 1.87 |
| Cu-4 | $N_2$ | 55 | $0.6{\cdot}L_o$ | 0.25 | 117 | 41.7 | 25.2 | 1.66 | 17 | 42 | 115 | 1.99 |
| Cu-5 | $N_2$ | 55 | $0.6{\cdot}L_o$ | 0.25 | 117 | 41.7 | 24.4 | 1.71 | 16 | 41 | 104 | 1.93 |
| Cu-6 | $N_2$ | 55 | $0.6{\cdot}L_o$ | 0.25 | 117 | 41.7 | 29.8 | 1.40 | 15 | 41 | 101 | 1.92 |
| Cu-7 | $N_2$ | 55 | $0.6{\cdot}L_o$ | 0.25 | 117 | 41.7 | 18.8 | 2.22 | 10 | 36 | 87 | 1.95 |
| Cu-8 | $N_2$ | 55 | $0.6{\cdot}L_o$ | 0.25 | 117 | 41.7 | 22.4 | 1.87 | 13 | 39 | 99 | 1.95 |
| Cu-9 | $N_2$ | 55 | $0.6{\cdot}L_o$ | 0.25 | 117 | 41.7 | 23.8 | 1.76 | 14 | 40 | 102 | 1.99 |
| Cu-10 | $N_2$ | 55 | $0.6{\cdot}L_o$ | 0.25 | 117 | 41.7 | 27.9 | 1.50 | 16 | 39 | 98 | 1.88 |
| Cu-11 | $N_2$ | 55 | $0.6{\cdot}L_o$ | 0.25 | 117 | 41.7 | 29.6 | 1.41 | 16 | 42 | 117 | 2.03 |
| Cu-12 | $N_2$ | 10 | $0.77{\cdot}L_o$ | – | 200 | 9.8 | 53.6 | 0.18 | – | – | – | – |
| Cu-13 | $N_2$ | 20 | $0.77{\cdot}L_o$ | – | 200 | 19.6 | 48.4 | 0.41 | 28 | 77 | 211 | 2.13 |
| Cu-14 | $N_2$ | 30 | $0.77{\cdot}L_o$ | – | 200 | 29.4 | 45.5 | 0.65 | 19 | 55 | 141 | 2.08 |
| Cu-15 | $N_2$ | 40 | $0.77{\cdot}L_o$ | – | 200 | 39.2 | 49.3 | 0.80 | 16 | 45 | 136 | 2.22 |
| Cu-16 | $N_2$ | 50 | $0.77{\cdot}L_o$ | – | 200 | 49.0 | 40.2 | 1.22 | 10 | 39 | 103 | 2.09 |
| Cu-17 | $N_2$ | 50 | $0.77{\cdot}L_o$ | – | 200 | 49.0 | 25.4 | 1.93 | 11 | 37 | 82 | 1.89 |
| Cu-18 | $N_2$ | 50 | $0.77{\cdot}L_o$ | – | 200 | 49.0 | 22.9 | 2.14 | 8 | 28 | 53 | 1.77 |
| Cu-19 | $N_2$ | 50 | $0.77{\cdot}L_o$ | – | 200 | 49.0 | 17.2 | 2.86 | 8 | 26 | 52 | 1.74 |
| Cu-20 | $N_2$ | 50 | $0.77{\cdot}L_o$ | – | 200 | 49.0 | 9.3 | 5.27 | 6 | 21 | 44 | 1.68 |
| Cu-21 | $N_2$ | 60 | $0.77{\cdot}L_o$ | – | 200 | 58.9 | – | – | – | – | – | – |
| Cu-22 | $N_2$ | 30 | $0.6{\cdot}L_o$ | 0.25 | 200 | 22.8 | 37.5 | 0.61 | 20 | 67 | 216 | 2.55 |
| Cu-23 | $N_2$ | 40 | $0.6{\cdot}L_o$ | 0.25 | 200 | 30.4 | 23.8 | 1.27 | 17 | 44 | 104 | 2.08 |
| Cu-24 | $N_2$ | 50 | $0.6{\cdot}L_o$ | 0.25 | 200 | 37.9 | 21.7 | 1.75 | 7 | 33 | 95 | 2.11 |
| Cu-25 | $N_2$ | 60 | $0.6{\cdot}L_o$ | 0.25 | 200 | 45.5 | 13.8 | 3.30 | 4 | 23 | 62 | 1.95 |
| Cu-26 | $N_2$ | 30 | $0.6{\cdot}L_o$ | 0.4 | 200 | 22.8 | 48.0 | 0.47 | 28 | 74 | 234 | 2.23 |
| Cu-27 | $N_2$ | 40 | $0.6{\cdot}L_o$ | 0.4 | 200 | 30.4 | 39.0 | 0.78 | 12 | 53 | 166 | 2.43 |
| Cu-28 | $N_2$ | 50 | $0.6{\cdot}L_o$ | 0.4 | 200 | 37.9 | 22.5 | 1.68 | 8 | 40 | 110 | 2.28 |
| Cu-29 | $N_2$ | 60 | $0.6{\cdot}L_o$ | 0.4 | 200 | 45.5 | 14.8 | 3.08 | 4 | 22 | 57 | 1.91 |
| Cu-30 | $N_2$ | 50 | $0.77{\cdot}L_o$ | 0.25 | 25 | 49.0 | – | – | – | – | – | – |

(*continued*)

| Atomisation | Gas | P (bar) | Throat width | ΔP* (bar) | ΔT (°C) | $m_g$ (g/s) | $m_m$ (g/s) | GMR | $D_{10}$ (μm) | $D_{50}$ (μm) | $D_{90}$ (μm) | $\sigma_{LN}$ |
|---|---|---|---|---|---|---|---|---|---|---|---|---|
| Cu-31 | $N_2$ | 50 | 0.77·$L_o$ | 0.25 | 55 | 49.0 | 39.1 | 1.25 | 21 | 51 | 130 | 1.95 |
| Cu-32 | $N_2$ | 50 | 0.77·$L_o$ | 0.25 | 100 | 49.0 | 38.8 | 1.26 | 13 | 43 | 104 | 2.01 |
| Cu-33 | $N_2$ | 50 | 0.77·$L_o$ | 0.25 | 500 | 49.0 | 40.5 | 1.21 | 12 | 41 | 108 | 2.09 |
| Cu-34 | Ar | 30 | 0.6·$L_o$ | 0.25 | 200 | 29.8 | 51.5 | 0.58 | 24 | 96 | 347 | 2.48 |
| Cu-35 | Ar | 40 | 0.6·$L_o$ | 0.25 | 200 | 39.8 | 29.8 | 1.34 | 14 | 58 | 148 | 2.33 |
| Cu-36 | Ar | 50 | 0.6·$L_o$ | 0.25 | 200 | 49.7 | 29.0 | 1.71 | 13 | 52 | 133 | 2.16 |
| Cu-37 | Ar | 60 | 0.6·$L_o$ | 0.25 | 200 | 59.6 | 12.0 | 4.99 | 9 | 30 | 65 | 1.91 |
| Cu-38 | He | 30 | 0.6·$L_o$ | 0.25 | 200 | 8.9 | 30.5 | 0.29 | 10 | 53 | 191 | 2.87 |
| Cu-39 | He | 40 | 0.6·$L_o$ | 0.25 | 200 | 11.8 | 35.9 | 0.33 | 7 | 42 | 165 | 3.00 |
| Cu-40 | He | 45 | 0.6·$L_o$ | 0.4 | 200 | 13.3 | 30.4 | 0.44 | 6 | 36 | 143 | 2.97 |
| Cu-41 | He | 50 | 0.6·$L_o$ | 0.25 | 200 | 14.8 | – | – | – | – | – | – |
| Cu-42 | He | 60 | 0.6·$L_o$ | 0.25 | 200 | 17.8 | – | – | – | – | – | – |
| Cu-43 | He | 60 | 0.6·$L_o$ | – | 350 | 17.8 | 31.2 | 0.57 | 5 | 18 | 46 | 1.99 |
| SS 316 L-1 | $N_2$ | 30 | 0.6·$L_o$ | 0.25 | 260 | 22.8 | 48.3 | 0.47 | 21 | 77 | 246 | 2.63 |
| SS 316 L-2 | $N_2$ | 45 | 0.6·$L_o$ | 0.25 | 260 | 34.1 | 13.6 | 2.52 | 8 | 37 | 103 | 2.29 |
| SS 316 L-3 | $N_2$ | 45 | 0.6·$L_o$ | 0.25 | 260 | 34.1 | 14.9 | 2.29 | 8 | 37 | 102 | 2.26 |
| SS 316 L-4 | $N_2$ | 60 | 0.6·$L_o$ | 0.25 | 260 | 45.5 | 11.4 | 3.98 | 7 | 32 | 79 | 2.13 |
| SS 316 L-5 | Ar | 60 | 0.6·$L_o$ | 0.25 | 260 | 59.6 | 11.6 | 5.13 | 7 | 33 | 83 | 2.17 |
| SS 316 L-6 | He | 60 | 0.6·$L_o$ | 0.25 | 260 | 17.8 | 25.2 | 0.71 | 5 | 26 | 82 | 2.27 |
| Sn-1 | $N_2$ | 20 | 0.77·$L_o$ | – | 74 | 19.6 | 80.6 | 0.24 | 32 | 82 | 214 | 2.18 |
| Sn-2 | $N_2$ | 30 | 0.77·$L_o$ | – | 74 | 29.4 | 63.0 | 0.47 | 25 | 56 | 137 | 1.94 |
| Sn-3 | $N_2$ | 50 | 0.77·$L_o$ | – | 186 | 49.0 | 27.9 | 1.76 | 5 | 15 | 38 | 2.16 |
| Sn-4 | $N_2$ | 30 | 0.6·$L_o$ | 0.25 | 74 | 22.8 | 35.9 | 0.63 | 11 | 44 | 105 | 2.04 |
| Sn-5 | $N_2$ | 45 | 0.6·$L_o$ | 0.25 | 74 | 34.1 | 23.2 | 1.47 | 8 | 24 | 53 | 1.89 |
| Sn-6 | $N_2$ | 60 | 0.6·$L_o$ | 0.25 | 74 | 45.5 | 14.2 | 3.22 | 4 | 13 | 35 | 1.99 |
| Sn-7 | $N_2$ | 60 | 0.6·$L_o$ | 0.25 | 200 | 45.5 | 28.5 | 1.60 | 4 | 14 | 44 | 2.17 |
| Sn-8 | $N_2$ | 60 | 0.6·$L_o$ | 0.25 | 500 | 45.5 | 14.2 | 3.20 | 3 | 10 | 23 | 1.36 |
| Fe-1 | $N_2$ | 44 | 0.91·$L_o$ | 0.25 | 165 | 52.0 | 32.2 | 1.61 | 9 | 39 | 102 | 2.18 |
| Fe-2 | $N_2$ | 60 | 0.6·$L_o$ | 0.25 | 165 | 45.5 | 24.5 | 1.86 | 6 | 33 | 74 | 1.98 |
| Fe-3 | Ar | 44 | 0.91·$L_o$ | 0.25 | 165 | 68.2 | 14.3 | 4.78 | 8 | 31 | 67 | 1.80 |
| Fe-4 | Ar | 60 | 0.6·$L_o$ | 0.25 | 165 | 59.6 | 18.5 | 3.22 | 9 | 36 | 79 | 1.98 |
| Fe-5 | He | 30 | 0.6·$L_o$ | 0.25 | 165 | 8.9 | – | – | – | – | – | – |
| Fe-6 | He | 50 | 0.6·$L_o$ | 0.25 | 165 | 14.8 | – | – | – | – | – | – |
| Fe-7 | He | 60 | 0.6·$L_o$ | 0.25 | 165 | 17.8 | – | – | – | – | – | – |
| Bronze-1 | $N_2$ | 30 | 0.77·$L_o$ | 0.25 | 179 | 29.4 | 44.1 | 0.67 | 12 | 42 | 157 | 2.76 |
| Bronze-2 | $N_2$ | 50 | 0.77·$L_o$ | 0.25 | 444 | 49.0 | 35.7 | 1.37 | 18 | 37 | 94 | 1.81 |

**ΔP*:** In some experiments, the overpressure applied to the melt is unknown because the aspiration pressure in the melt feed tube was not measured before the atomisation.

## References


[1] L. Achelis, V. Uhlenwinkel, Characterisation of metal powders generated by a pressure-gas-atomiser, Mater. Sci. Eng. A 477 (2008) 15–20, https://doi.org/10.1016/j.msea.2007.07.095.

[2] K.L. Alvarez, H.A. Baghbaderani, J.M. Martín, N. Burgos, M. Ipatov, Z. Pavlovic, P. McCloskey, A. Masood, J. Gonzalez, Novel Fe-based amorphous and nanocrystalline powder cores for high-frequency power conversion, J. Magn. Magn. Mater. 501 (2020) https://doi.org/10.1016/j.jmmm.2020.166457.

[3] I.E. Anderson, R.S. Figliola, R.L. Terpstra, S. Rau, B. Rauscher, Progress in experimental analysis of gas atomization process physics, in: proceedings of the 2002 world congress on Powder Metallurgy & Particulate Materials. Metal powder industries federation (MPIF), Orlando, USA, 2002 150–162.

[4] Ansys Incorporated, Ansys Fluent 2020 R1 User's guide, 2020.

[5] J.D. Ayers, I.E. Anderson, Very fine metal powders, JOM 37 (1985) 16–21, https://doi.org/10.1007/BF03257673.

[6] M.J. Carrington, J. Daure, V.L. Ratia, P.H. Shipway, D.G. McCartney, D.A. Stewart, Microstructural characterisation of Tristelle 5183 (Fe-21%Cr-10%Ni-7.5%Nb-5%Si-2%C in wt%) alloy powder produced by gas atomisation, Mater. Des. 164 (2019) https://doi.org/10.1016/j.matdes.2018.107548.

[7] J.J. Dunkley, The role of energy in gas atomisation, Proceedings of the 2001 international conference on Powder Metallurgy & Particulate Materials. Metal powder industries federation (MPIF), New Orleans, USA 2001, pp. 133–139.

[8] H. Fukuyama, H. Higashi, H. Yamano, Thermophysical properties of molten stainless steel containing 5 mass % B 4 C, Nucl. Technol. 205 (2019) 1154–1163, https://doi.org/10.1080/00295450.2019.1578572.

[9] R.M. German, Powder Metallurgy and Particulate Materials Processing: The Processes, Materials, Products, Properties and Applications, Metal Powder Industries Federation (MPIF), Princeton, New Jersey, USA, 2005.

[10] K. Hanthanan Arachchilage, M. Haghshenas, S. Park, L. Zhou, Y. Sohn, B. McWilliams, K. Cho, R. Kumar, Numerical simulation of high-pressure gas atomization of two-phase flow: effect of gas pressure on droplet size distribution, Adv. Powder Technol. 30 (2019) 2726–2732, https://doi.org/10.1016/j.apt.2019.08.019.

[11] T. Iida, R.I.L. Guthrie, The Physical Properties of Liquid Metal, Clarendon Press, Oxford, UK, 1988.

[12] H. Kishidaka, Theory and Production of Atomized Iron Powder, in: Proceedings of the Multidisciplinary Meeting on Sintered Metals and Magnetic Materials, Japan Society for Powder and Powder Metallurgy, Japan, 1972 19–24.

[13] J. Lee, W. Shimoda, T. Tanaka, Surface tension and its temperature coefficient of liquid Sn-X (X=Ag, cu) alloys, Mater. Trans. 45 (2004) 2864–2870, https://doi.org/10.2320/matertrans.45.2864.

[14] H. Lubanska, Correlation of spray ring data for gas atomization of liquid metals, JOM 22 (1970) 45–49, https://doi.org/10.1007/BF03355938.

[15] J.E. MacDonald, R.H.U. Khan, M. Aristizabal, K.E.A. Essa, M.J. Lunt, M.M. Attallah, Influence of powder characteristics on the microstructure and mechanical properties of HIPped CM247LC Ni superalloy, Mater. Des. 174 (2019) 1–11, https://doi.org/10.1016/j.matdes.2019.107796.

[16] S.P. Mates, S.D. Ridder, F.S. Biancaniello, Comparison of the Supersonic Length and Dynamic Pressure Characteristics of Discrete-Jet and Annular Close-Coupled Nozzles Used to Produce Fine Metal Powders, in: Proceedings of the 129th Annual Meeting & Exhibition of the Minerals, Metals & Materials Society. Nashville, USA, 2000 71–81.

[17] S.P. Mates, G.S. Settles, A study of liquid metal atomization using close-coupled nozzles, part 1: gas dynamic behavior, At. Sprays 15 (2005) 19–40, https://doi.org/10.1615/AtomizSpr.v15.i1.20.

[18] S.P. Mates, G.S. Settles, A study of liquid metal atomization using close-coupled nozzles, part 2: atomization behavior, At. Sprays 15 (2005) 41–60, https://doi.org/10.1615/AtomizSpr.v15.i1.30.

[19] Mathworks Incorporated, Matlab R2020a User's Manual, 2020.

[20] Metal Powder Industries Federation (MPIF), MPIF 05 Determination of Sieve Analysis of Metal Powders, 1992.

[21] R.S. Miller, S.A. Miller, S.D. Savkar, D.P. Mourer, Two phase flow model for the close-coupled atomization of metals, Proceedings of the 1996 international powder metallurgy conference 1996, pp. 341–352.

[22] A.M. Mullis, I.N. McCarthy, R.F. Cochrane, High speed imaging of the flow during close-coupled gas atomisation: effect of melt delivery nozzle geometry, J. Mater. Process. Technol. 211 (2011) 1471–1477, https://doi.org/10.1016/j.jmatprotec.2011.03.020.

[23] H. Ouyang, X. Chen, B. Huang, Influence of melt superheat on breakup process of close-coupled gas atomization, Trans. Nonferrous Metals Soc. China 17 (2007) 967–973, https://doi.org/10.1016/S1003-6326(07)60209-X.

[24] K.P. Rao, S.P. Mehrotra, Effect of process variables on atomization of metals and alloys, Modern Developments in Powder Metallurgy. Metal Powder Industries Federation (MPIF) 1981, pp. 113–130.

[25] M.H. Saleh, F. Ismail, N. Muhamad, Gas atomization of fine aluminum alloy powder for metal injection molding, Proceedings of the 3rd International Powder Metallurgy Conference. Turkish Powder Metallurgy Association (TTMD), Ankara, Turkey 2002, pp. 326–336.
[26] Y. Sato, K. Sugisawa, D. Aoki, T. Yamamura, Viscosities of Fe–Ni, Fe–co and Ni–co binary melts, Meas. Sci. Technol. 16 (2005) 363–371, https://doi.org/10.1088/0957-0233/16/2/006.
[27] U. Scipioni Bertoli, G. Guss, S. Wu, M.J. Matthews, J.M. Schoenung, In-situ characterization of laser-powder interaction and cooling rates through high-speed imaging of powder bed fusion additive manufacturing, Mater. Des. 135 (2017) 385–396, https://doi.org/10.1016/j.matdes.2017.09.044.
[28] H.E. Snyder, D.W. Senser, A.H. Lefebvre, Mean drop sizes from fan spray atomizers, J. Fluids Eng. 111 (1989) 342–347, https://doi.org/10.1115/1.3243650.
[29] R. Tamura, T. Osada, K. Minagawa, T. Kohata, M. Hirosawa, K. Tsuda, K. Kawagishi, Machine learning-driven optimization in powder manufacturing of Ni co based superalloy, Mater. Des. 109290 (2020) https://doi.org/10.1016/j.matdes.2020.109290.
[30] M. Tan, B. Xiufang, X. Xianying, Z. Yanning, G. Jing, S. Baoan, Correlation between viscosity of molten cu–Sn alloys and phase diagram, Phys. B Condens. Matter 387 (2007) 1–5, https://doi.org/10.1016/j.physb.2005.10.140.
[31] J. Ting, J. Connor, S. Ridder, High-speed cinematography of gas-metal atomization, Mater. Sci. Eng. A 390 (2005) 452–460, https://doi.org/10.1016/j.msea.2004.08.060.
[32] J. Ting, M.W. Peretti, W.B. Eisen, The effect of wake-closure phenomenon on gas atomization performance, Mater. Sci. Eng. A 326 (2002) 110–121, https://doi.org/10.1016/S0921-5093(01)01437-X.
[33] A. Ünal, Effect of processing variables on particle size in gas atomization of rapidly solidified aluminium powders, Mater. Sci. Technol. 3 (1987) 1029–1039, https://doi.org/10.1179/mst.1987.3.12.1029.
[34] R. Ünal, The influence of the pressure formation at the tip of the melt delivery tube on tin powder size and gas/melt ratio in gas atomization method, J. Mater. Process. Technol. 180 (2006) 291–295, https://doi.org/10.1016/j.jmatprotec.2006.06.018.
[35] E. Urionabarrenetxea, J.M. Martín, A. Rivas, I. Iturriza, F. Castro, Influence of key operational and geometrical variables on the particle size during close-coupled gas atomisation, Proceedings of the International Powder Metallurgy Congress and Exhibition, Euro PM 2014, European Powder Metallurgy Association (EPMA), Salzburg, Germany, 2014.
[36] E. Urionabarrenetxea, J.M. Martín, A. Rivas, I. Iturriza, F. Castro, Experimental study and simulation of the gas flow in the atomisation chamber during close-coupled gas atomisation, Proceedings of the International Powder Metallurgy Congress and Exhibition, Euro PM 2013, European Powder Metallurgy Association (EPMA), Gothenburg, Sweden 2013, pp. 257–262.
[37] P. Wang, P. Huang, F.L. Ng, W.J. Sin, S. Lu, M.L.S. Nai, Z.L. Dong, J. Wei, Additively manufactured CoCrFeNiMn high-entropy alloy via pre-alloyed powder, Mater. Des. 168 (2019) https://doi.org/10.1016/j.matdes.2018.107576.
[38] M. Wei, S. Chen, M. Sun, J. Liang, C. Liu, M. Wang, Atomization simulation and preparation of 24CrNiMoY alloy steel powder using VIGA technology at high gas pressure, Powder Technol. (2020) https://doi.org/10.1016/j.powtec.2020.04.030.
[39] N. Zeoli, S. Gu, Computational validation of an isentropic plug nozzle design for gas atomisation, Comput. Mater. Sci. 42 (2008) 245–258, https://doi.org/10.1016/j.commatsci.2007.07.013.
[40] Y. Zhang, J. Zhang, Modeling of solidification microstructure evolution in laser powder bed fusion fabricated 316L stainless steel using combined computational fluid dynamics and cellular automata, Addit. Manuf. 28 (2019) 750–765, https://doi.org/10.1016/j.addma.2019.06.024.
[41] B. Zheng, Y. Lin, Y. Zhou, E.J. Lavernia, Gas atomization of amorphous aluminum: part I, Thermal Behavior Calculations. Metall. Mater. Trans. B 40 (2009) 768–778, https://doi.org/10.1007/s11663-009-9276-5.